

Treating produced water from hydraulic fracturing: composition effects on scale formation and desalination system selection

Gregory P. Thiel^a, John H. Lienhard V^{a,*}

^a*Rohsenow Kendall Heat Transfer Laboratory, Department of Mechanical Engineering, Massachusetts Institute of Technology, Cambridge, MA 02139-4307, USA*

Abstract

Produced water from unconventional gas and oil extraction may be hypersaline with uncommon combinations of dissolved ions. The aim of this analysis is to aid in the selection of produced water treatment technology by identifying the temperature, pH, and recovery ratio under which mineral solid formation from these produced waters is likely to occur. Eight samples of produced water from the Permian Basin and the Marcellus shale are discussed, with an average TDS of about 177 g/L but significant variability. Crystallization potential is quantified by the saturation index, and activity coefficients are calculated using the Pitzer model. The method is applied to estimate solid formation in the treatment of two design case samples: a 183 g/L sample representing the Permian Basin water and a 145 g/L sample representing the Marcellus. Without pretreatment, the most likely solids to form, defined by highest saturation index, are: CaCO₃, FeCO₃, MgCO₃, MnCO₃, SrCO₃, BaSO₄, CaSO₄, MgSO₄ and SrSO₄. Some options for mitigating the formation of these scales are discussed. With appropriate pretreatment, it is estimated that recovery ratios of as high as 40–50% are achievable before NaCl, a major constituent, is likely to limit further concentration without significant crystallization.

Keywords: wastewater treatment; scaling; fracking; frack water; Marcellus; Permian Basin

*Corresponding author

Email address: lienhard@mit.edu (John H. Lienhard V)

Nomenclature

Roman Symbols

a	Activity
A^ϕ	Modified Debye-Hückel parameter, $\text{kg}^{1/2}/\text{mol}^{1/2}$
B_{ij}, B_{ij}^ϕ	Pitzer parameter, second virial coefficient, kg/mol
B'_{ij}	Pitzer binary interaction parameter, kg^2/mol^2
c	Concentration, mol/L
C_{ij}, C_{ij}^ϕ	Pitzer parameter, unlike-charged interactions, kg^2/mol^2
C_P	Molar heat capacity, $\text{J}/\text{mol}\cdot\text{K}$
e	Fundamental charge, C
F	Extended Debye-Hückel function, Eq. (B.1)
g, g'	Pitzer function, Eqs. (B.7) and (B.8)
G	Gibbs free energy, kJ/mol
H	Enthalpy, kJ/mol
I	Ionic strength, mol/kg
K	Equilibrium constant
k_B	Boltzmann's constant, J/K
K_{sp}	Solubility product
m	Molality, mol/kg
M	Molar mass, g/mol
\dot{m}	Mass flow rate, kg/s
N_A	Avogadro's number, mol^{-1}
Q	Activity product (Reaction quotient)
R	Universal gas constant, $\text{kJ}/\text{mol}\cdot\text{K}$
RR	Recovery ratio
S	Supersaturation ratio
SI	Saturation index, $\log(Q/K_{sp})$
T	Temperature, $^\circ\text{C}$ or K
TDS	Total dissolved solids, mg/L or mg/kg
w	Mass fraction
z	Charge number
Z	Pitzer function, $\sum_i m_i z_i $, mol/kg

Greek Symbols

α	Pitzer parameter, $\text{kg}^{1/2}/\text{mol}^{1/2}$
β	Pitzer parameter, kg/mol

γ	Molal activity coefficient
Δ	Change
Δ_r	Change of reaction
Δ_f	Change of formation
ε	Relative permittivity
θ	Pitzer parameter, kg/mol
λ_{ij}	Pitzer parameter, uncharged interactions, kg/mol
μ	Chemical potential, kJ/mol
ν	Stoichiometric coefficient
ξ	Dummy variable
ρ	Density, kg/L
σ	Supersaturation (percent)
ϕ	Osmotic coefficient
$\Phi_{ij}, \Phi_{ij}^\phi$	Pitzer parameter, like-charged interactions, kg/mol
Φ'_{ij}	Pitzer parameter, like-charged interactions, kg ² /mol ²
Ψ_{ijk}	Pitzer parameter, ternary interactions, kg ² /mol ²

Subscripts

a, X	Anion
b	Brine stream
c, M	Cation
f	Feed stream
n, N	Neutral species
p	Product water stream
s	Solvent
sat	Saturated
T	Total
W	Water

Superscripts

\circ	Reference state
---------	-----------------

1. Introduction

Owing to recent advances in drilling technology and increasing global demand, the use of hydraulic fracturing to recover abundant supplies of oil and natural gas in shale has become economically feasible. According to the U.S. Energy Information Administration (EIA) [1, 2], nearly 207 trillion cubic meters (7,299 tcf) of natural gas and 55 billion cubic meters (345 billion barrels) of oil are technically recoverable—a near sixty-year supply of gas and a decade-long supply of oil at current rates of global consumption.

Although not a renewable resource, natural gas provides significant environmental benefits over other widely available fossil fuels. In particular, according the U.S. Environmental Protection Agency (EPA), natural gas powerplants produce half as much carbon dioxide as a typical coal powerplant, and harmful emissions of nitrous oxides and sulfur oxides are reduced by 66% and 99%, respectively [3]. Mercury emissions are effectively eliminated.

Hydraulic fracturing works as follows. A well is drilled vertically down into a narrow shale layer (as narrow as 50 m [4]) at a depth of anywhere from 1200 to 3600 m. The drill is then turned and proceeds horizontally into the shale layer. A high pressure mixture of water, sand, and chemicals (about 84%, 15%, and 1% by mass, respectively) is then pumped into the well to create microfissures in, or to fracture the shale [4, 5]. The sand acts as a “proppant,” holding these microfissures open and allowing a continuous stream of hydrocarbons and associated water to escape up the well.

About 15–25% of the fluid pumped down to fracture the well will return to the surface as “flowback” at relatively high flow rates and relatively low total dissolved solids (TDS). After approximately one to three weeks [6], the flow of water decreases significantly and the TDS increases sharply; this subsequent stream is known as produced water and will continue to flow throughout the life of the well. Produced water can be hypersaline, as it may have up to nine times the salinity of seawater [4]. Flowback can often be reused in subsequent fracturing operations [7], whereas in general produced water cannot and must be treated or disposed of.

According to a report prepared by Argonne National Laboratory and the U. S. Department of Energy, the total volume of produced water from all U. S. oil and gas production is 2.5 trillion cubic meters per year [8]. Accounting for the portion of this attributable to unconventional gas production is difficult, but average federal, onshore water-to-gas ratios are estimated at about 1.46 L/m³ [8], and according to the EIA [1], tight gas and shale gas together accounted for nearly 60% of U. S. natural gas production in 2011, or about 388 billion cubic meters of gas. We might therefore estimate of U. S. produced water generation to be approximately 566 million cubic meters per year.

Despite the promise of hydraulic fracturing, the disposal of these large quantities of produced water is among the most significant barriers to expanded use of the process. Conventional disposal procedures involve transporting this wastewater to a disposal well [7], where it is reinjected into the ground. Unfortunately, this process is fraught with difficulties arising from environmental and geological concerns, local regulatory framework, and high transportation costs. Environmentally, the disposal of wastewater via deep well injec-

tion has been linked to significantly increased seismicity [9], including cases in Arkansas [10], Ohio [11], and Oklahoma [12]. In the Marcellus, a combination of regulatory issues and geological conditions in Pennsylvania make wastewater disposal via deep-well injection infeasible. Operators in the Marcellus consequently transport the water across state lines, to Ohio, where far more injection wells are available [13]. Economically, trucking costs are a strong function of the distance from the well to the disposal site and are significant—typically \$25 per m³ (\$4 per bbl) in the Marcellus [14].

One potential solution addressing both economic and environmental concerns is *in situ* desalination. However, the selection of appropriate treatment technologies proves challenging as a result of: (1) the difficulty in characterizing mixed-electrolytes of high ionic strength; (2) the desirability of high recovery ratios; and (3) significant variations in water composition from formation to formation and even well to well. In this work, original data on produced water samples from the Marcellus Shale in New York and Pennsylvania and from the Permian Basin in Texas are presented and analyzed. A method for water sample analysis is developed, and the thermophysical conditions under which treatment using conventional desalination systems is feasible are identified. Finally, as a consequence of these analyses, some general recommendations on treatment options are presented.

2. Produced Water Samples

Three samples of produced water from the Permian Basin in Texas and five samples from the Marcellus in Pennsylvania and New York were assayed. Water sample analyses were performed by Microbac Laboratories, Inc. of Worcester, Massachusetts. Each sample was tested for 27 potential dissolved compounds: aluminum, arsenic, barium, beryllium, bicarbonate, boron, bromide, cadmium, calcium, chloride, chromium, cobalt, copper, iron, lead, lithium, magnesium, manganese, mercury, molybdenum, nickel, potassium, selenium, silver, sodium, strontium, and sulfate.

The results are shown in Table 1. The total dissolved solids (TDS) varies widely, ranging from a low of about 120 g/L to a high of nearly 250 g/L. In addition, individual ion concentrations can vary significantly: in Permian Basin sample 2, the concentrations of Mn²⁺ and K⁺ differ by a factor of about 2 and 4, respectively, from the other two samples from the Permian Basin. Concentrations are not given where the result is lower than the resolution of the test.

Unfortunately, data on dissolved silica, a common scale-forming compound, is unavailable from our samples. Other samples of Marcellus wastewater in open literature [6] show silica concentrations between 10 and 40 mg/L; in the Permian it is generally between 50 and 150 mg/L. With silica solubility between 100 and 150 mg/L at room temperature [15], it may be problematic in the Permian, but appears less likely to be so in the Marcellus.

Any organic carbon may also have an impact on ion speciation and mineral solubilities, although this impact is considered negligible in seawater [16]. Total organic carbon (TOC) data from our samples is unavailable, but TOC data from [6] range from < 10 to 160 mg/L, and will at least in part depend on the

Table 1: Composition of water samples of produced water from unconventional oil and gas processes in the Permian Basin and the Marcellus

Species	Sample Concentration (mg/L)							
	Permian Basin			Marcellus				
	No. 1	No. 2	No. 3	No. 1	No. 2	No. 3	No. 4	No. 5
Br ⁻	1,160	1,650	1,370	541	1,820	872	1,100	1,678
Ba ²⁺	16	0	16	9,700	9,400	8,900	2,800	8,923
Ca ²⁺	14,000	10,000	15,000	5,400	23,000	7,600	13,000	13,875
Cl ⁻	116,000	111,000	138,000	66,600	157,000	91,200	82,800	115,194
Co ²⁺ , Co ³⁺	-	-	-	8	8.2	6.8	-	-
Fe ²⁺ , Fe ³⁺	-	-	-	120	24	53	20	-
HCO ₃ ⁻	108	92	160	48	-	-	-	-
K ⁺	840	570	1,100	160	430	110	310	-
Li ⁺	-	-	-	130	170	85	90	369
Mg ²⁺	1,650	1,630	1,950	492	1,690	754	1,380	1,216
Mn ²⁺	42	11	53	6.9	9.3	-	5.1	4
Na ⁺	54,000	48,000	54,000	33,000	46,000	33,000	31,000	46,695
SO ₄ ²⁻	743	530	515	1,500	1,040	550	-	26
Sr ²⁺	740	730	820	2,700	7,700	3,300	3,000	4,064
TDS	189,299	174,213	212,984	120,406	248,292	146,431	135,505	192,044

method used for oil-water separation. Moreover, its effects on the solubilities of the compounds considered here would be difficult to quantify without knowing the makeup of the TOC. We thus do not consider the effects further.

To capture the essential makeup of each region’s produced water, a design-case sample was created by averaging over the three samples in Table 1 with some adjustments to maintain electroneutrality and to ensure no compounds were supersaturated at ambient conditions. The design-case data for both regions are shown in Table 2. In each of the samples in Table 1, the maximum and minimum concentrations of individual ions generally vary by less than about 30–40% relative to their design case values in Table 2; however, some compounds (particularly iron, cobalt, sulfate, and strontium in the Marcellus) vary significantly more.

Three additional approximations were employed in the construction of the design-case from the field data. First, the water samples’ pH are unavailable. Based on data from other hydraulic fracturing water literature (e.g., [6]), the pH is generally neutral to slightly acidic; we therefore assume a baseline pH of 6. (The pH is varied in model.) Second, in the sample tests, dissolved inorganic carbon was reported as the concentration of HCO₃⁻; in the design case it is quantified as total inorganic carbon, C_T, which is preferable particularly when pH data are unavailable. Third, the sample tests do not distinguish between Fe²⁺ and Fe³⁺ or between Co²⁺ and Co³⁺: absent data on dissolved oxygen concentrations, we cannot determine the relative proportions of either. We thus consider only the 2+ forms here.

Table 2: Composition of design-case produced water samples

Species	Concentration			
	Permian Basin		Marcellus	
	mg/L	millimolal	mg/L	millimolal
Br ⁻	1,393	18.8	1,202	15.4
Ba ²⁺	0.453	0.00356	0.268	0.00200
Ca ²⁺	13,000	350	12,575	322
Cl ⁻	111,000	3,378	86,457	2,500
Co ²⁺	–	–	6	0.104
C _T	120	2.12	48	0.807
Fe ²⁺	–	–	54	1.00
K ⁺	837	23.1	253	6.63
Li ⁺	–	–	169	25.0
Mg ²⁺	1,743	77.4	1,106	46.7
Mn ²⁺	35	1.51	6	0.246
Na ⁺	53,550	2,513	37,939	1,692
SO ₄ ²⁻	596	6.69	779	8.32
Sr ²⁺	763	9.40	4,153	48.6
TDS	183,037	6,379	144,748	4,667

3. Method of Sample Analysis

The goal of this analysis is to predict the onset of supersaturation for binary compounds (i.e., single salts and bases) during the treatment of the design-case produced waters as a function of the operating temperature, pH, and recovery ratio of the treatment system. In this section, a thermodynamically natural measure of supersaturation is introduced and a method for its calculation is presented. A brief validation of the model is provided at the end of the section.

3.1. Quantifying Supersaturation

The driving force for crystallization is supersaturation. Many definitions exist in the literature, notably a difference, a ratio, and a percent:

$$\Delta c = c - c_{\text{sat}} \quad (1a)$$

$$S = \frac{c}{c_{\text{sat}}} \quad (1b)$$

$$\sigma = \frac{c - c_{\text{sat}}}{c_{\text{sat}}} \quad (1c)$$

Despite the intuitive value and the ease of calculation of these metrics, an alternative formulation, the saturation index, proves to be the most thermodynamically natural. Moreover, the solubility c_{sat} is generally unknown for any given compound in an arbitrary mixed electrolyte. The saturation index is:

$$\text{SI} = \log \left(\frac{Q}{K_{sp}} \right) = \log \left(\frac{a_M^{\nu_M} a_X^{\nu_X} a_W^{\nu_W}}{K_{sp}} \right) \quad (2)$$

where Q is the activity product, K_{sp} is the solubility product, a_i is the activity, ν is the stoichiometric coefficient, and the subscripts M , X , and W denote cation, anion, and hydrated water, respectively. When

SI < 0, the solution is subsaturated and any solid phase salt tends to dissolve; when SI > 0, the solution phase salt tends to crystallize. The rate of crystallization is governed by a combination of factors, although salts tend to crystallize more quickly at higher SI than at lower SI, and some compounds can remain in a metastable, solution-phase supersaturated state for a period of time (known as the induction time). For a 1-1 electrolyte, when the activity coefficients are one, the saturation index reduces to $SI = \log(S^2)$. The saturation index is well known but not universally employed; for this reason, a brief derivation is given in [Appendix A](#).

3.2. Calculating the Saturation Index

Because chemical equilibrium defines concentrations of individual species, but activity coefficients depend on concentration, the evaluation of Eq. (2) for any arbitrary state is an iterative process. The general process is to compute the activities of all aqueous species present in the water sample (including any relevant complexes), to identify possible solid-forming compounds, and to compute the saturation index, as shown in the flowchart (Figure 1). All calculations were performed in MATLAB.

3.2.1. Activity Coefficients

Activity coefficients are computed using the Pitzer model [17, 18], extended by Harvie and Weare [19] and Harvie et al. [20]. The model is based on a virial expansion of the excess Gibbs free energy, and takes into account binary and ternary ion interactions. The final equations employed in the present work are given below. Detailed derivations are given in references [17, 18, 21]. The model has been validated and used for calculations in several mixed electrolytes, e.g., [22, 23], and has been used successfully in the prediction of mineral solubilities in natural waters [20, 24].

The activity coefficient of an individual cation, M , is given by

$$\begin{aligned}
 \ln \gamma_M = & z_M^2 F + \sum_a m_a (2B_{Ma} + ZC_{Ma}) \\
 & + \sum_c m_c (2\Phi_{Mc} + \sum_a m_a \Psi_{Mca}) \\
 & + \sum_{a < a'} \sum m_a m_{a'} \Psi_{aa'M} \\
 & + |z_M| \sum_c \sum_a m_c m_a C_{ca} + \sum_n m_n (2\lambda_{nM})
 \end{aligned} \tag{3}$$

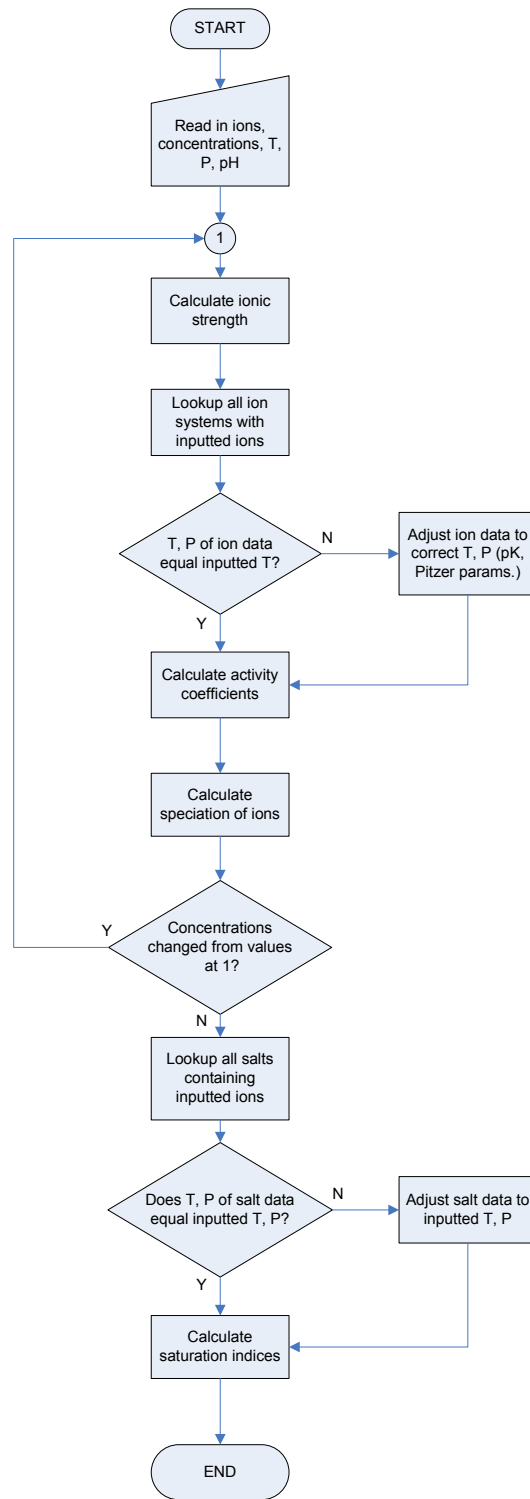


Figure 1: Calculation procedure for the saturation index, Eq. (2)

For an individual anion, X , the expression is analogous¹:

$$\begin{aligned}
\ln \gamma_X &= z_X^2 F + \sum_c m_c (2B_{cX} + ZC_{cX}) \\
&+ \sum_a m_a (2\Phi_{Xa} + \sum_c m_c \Psi_{Xac}) \\
&+ \sum_{c < c'} \sum m_c m_{c'} \Psi_{cc'X} \\
&+ |z_X| \sum_c \sum_a m_c m_a C_{ca} + \sum_n m_n (2\lambda_{nX})
\end{aligned} \tag{4}$$

The activity coefficient of uncharged species N (e.g., aqueous CO_2) is

$$\ln \gamma_N = \sum_c m_c (2\lambda_{Nc}) + \sum_a m_a (2\lambda_{Na}) \tag{5}$$

The activity of water is given by

$$\ln a_W = -\frac{M_W \sum_i m_i}{1000} \phi \tag{6}$$

where the osmotic coefficient ϕ is calculated from the expression

$$\begin{aligned}
(\phi - 1) \sum_i m_i &= 2 \left[\frac{-A^\phi I^{3/2}}{1 + 1.2\sqrt{I}} \right. \\
&+ \sum_c \sum_a m_c m_a (B_{ca}^\phi + ZC_{ca}) \\
&+ \sum_{c < c'} \sum m_c m_{c'} \left(\Phi_{cc'}^\phi + \sum_a m_a \Psi_{cc'a} \right) \\
&+ \sum_{a < a'} \sum m_a m_{a'} \left(\Phi_{aa'}^\phi + \sum_c m_c \Psi_{aa'c} \right) \\
&\left. + \sum_n \sum_a m_n m_a \lambda_{na} + \sum_n \sum_c m_n m_c \lambda_{nc} \right]
\end{aligned} \tag{7}$$

in which z is the charge number, m is molality, $I = \frac{1}{2} \sum_i m_i z_i^2$ is ionic strength, $Z = \sum_i |z_i| m_i$, M_W is the molar mass of water, and the remainder are functions quantifying particular solute interactions, as defined below. Subscript c denotes cations other than M , a denotes anions other than X , and n denotes neutral (uncharged) solutes. Summation over all i indicates a sum over all solutes; likewise summation over all c , a , and n denotes a sum over all cations, anions, and neutral solutes, respectively. The summation notations $c < c'$ and $a < a'$ indicate that the sum should be performed over all distinguishable cation pairs and anion pairs, respectively. Equations for A^ϕ , B_{ij} , B_{ij}^ϕ , F , Φ_{ij} , and Φ_{ij}^ϕ are given in [Appendix B](#).

In summary, the adjustable parameters are as follows. There are 3–4 per unlike-charged pair, $\beta_{MX}^{(0)}$, $\beta_{MX}^{(1)}$, $\beta_{MX}^{(2)}$, and C_{MX}^ϕ ; one per like-charged pair, θ_{ij} ; and one per cation-cation-anion and anion-anion-

¹Of course, as the activity of an individual ion cannot be measured explicitly, the physical meaning of such expressions is unclear. However, as noted by [19], the combination of Eqs. (3) and (4) in the form of a measurable mean activity coefficient produces the same equation as Pitzer [18], and is far more convenient for calculations in mixed electrolytes.

cation triplet, Ψ_{ijk} . The values of these parameters can be found in a variety of sources, some of which contain slightly different values. The values used here are from [20, 22, 25].

A complete set of parameters for all the aqueous species and combinations relevant to the present water samples is unavailable. This results from a lack of experimental thermodynamic data on certain electrolytes and from the difficulty of characterizing certain compounds with specific ion-interaction models like Pitzer’s (see Sec. 3.2.4), particularly at very high ionic strengths. Nevertheless, reasonable predictions of SI can often be made in the absence of specific interaction parameters when important ion complexes are included.

In addition, the temperature dependence of the Pitzer parameters themselves—but not the activity coefficient—is neglected. In principle, each of the adjustable binary and ternary parameters ($\beta_{MX}^{(i)}$, C_{MX}^ϕ , θ_{ij} , and Ψ_{ijk}) are functions of temperature. Unfortunately, a complete set of these data as a function of temperature over the range of interest are generally unavailable in open literature (although some significant collections are available, e.g. [18, 24, 26]). However, Silvester and Pitzer have noted that the temperature derivatives of these parameters are often small [27], and much of the temperature variation in activity coefficient is confined to A^ϕ (Eq. (B.2)) both in the parameter’s explicit temperature dependence, as well as implicitly through variations in the dielectric constant [28]. In addition, solubility predictions by DeLima and Pitzer [29] were not impaired by using room temperature values for the mixing parameters (θ_{ij} and Ψ_{ijk}) up to 473 K—well outside the temperature range of importance to this work. Because the data for the temperature dependence of the Pitzer parameters is relatively sparse over the range of interest here, to be consistent among electrolytes, only the values at 25 °C have been used. The effects of temperature on activity coefficient are thus approximate, and only captured by the variation of A^ϕ .

Finally, certain complexes are explicitly recognized when the solid-liquid equilibrium cannot be satisfactorily modeled using specific-ion interaction parameters alone (see Sec. 3.2.4). An evaluation of the error induced by these three approximations is given in Sec. 3.3.

3.2.2. Recovery Ratio

The recovery ratio is the mass of pure water obtained per unit mass of saline feed

$$\text{RR} = \frac{\dot{m}_p}{\dot{m}_f} \tag{8}$$

where \dot{m}_p and \dot{m}_f are the mass flow rates of product and feed, respectively. The effect of recovery ratio is manifested both explicitly in the increase in concentration of the ions as solvent is removed in a typical desalination process, as well as implicitly, through the effect of increased ion-ion interactions on the activity coefficient at higher values of ionic strength. The change in molality of an ion as a function of recovery ratio is given by

$$\frac{m_{i,b}}{m_{i,f}} = \frac{1}{1 - \text{RR}/w_{W,f}} \tag{9}$$

where $m_{i,b}$ and $m_{i,f}$ are the molalities of solute i in the brine and feed streams, respectively, and $w_{W,f}$ is the mass fraction of solvent (pure water) in the feed.

3.2.3. Equilibrium Constants

For relevant aqueous and solubility equilibria, the thermodynamic equilibrium constants are computed in the usual way:

$$K = \exp\left(-\frac{\Delta_r G^\circ}{RT}\right) \quad (10)$$

where the free energy change of reaction is defined as

$$\Delta_r G^\circ = \sum_i \nu_i \mu_i^\circ \quad (11)$$

where μ_i° is the standard state chemical potential. The standard state for the solid species is 25 °C and 1 bar. For aqueous species, the standard state is 25 °C and 1 bar and a hypothetical solution of unit activity at 1 molal. Equation (11) is evaluated using values of the Gibbs free energy of formation tabulated from a variety of sources; the values and their references employed here are tabulated in [Appendix C](#).

The temperature dependence of these equilibrium constants are given by van t'Hoff's law:

$$\frac{d(\ln K)}{dT} = -\frac{\Delta_r H}{RT^2} \quad (12)$$

At constant pressure, $\Delta_r H(T) = \Delta_r H^\circ + \int_{T^\circ}^T \Delta_r C_P d\xi$. Approximating $\Delta_r C_P$ as a constant, Eq. (12) is integrable, and results in the following temperature dependence of the equilibrium constant:

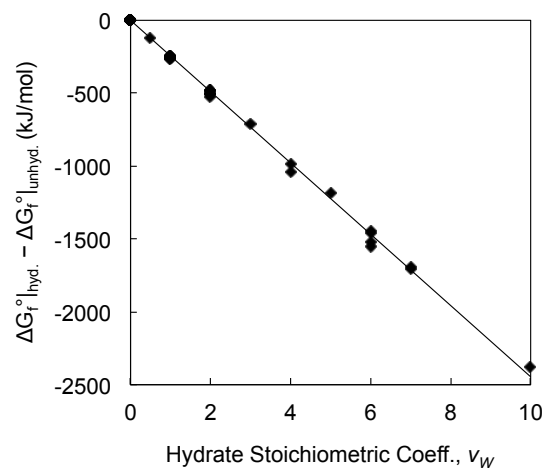
$$\begin{aligned} \ln\left(\frac{K}{K^\circ}\right) &= -\frac{\Delta_r H^\circ}{R} \left(\frac{1}{T} - \frac{1}{T^\circ}\right) \\ &+ \frac{\Delta_r C_P^\circ}{R} \left[\ln\left(\frac{T}{T^\circ}\right) - 1 + \left(\frac{T^\circ}{T}\right)\right] \end{aligned} \quad (13)$$

When no $\Delta_r C_P$ data are available, the second term in Eq. (13) is neglected. Measured data for the self-ionization constant of water as a function of temperature are from [\[30\]](#).

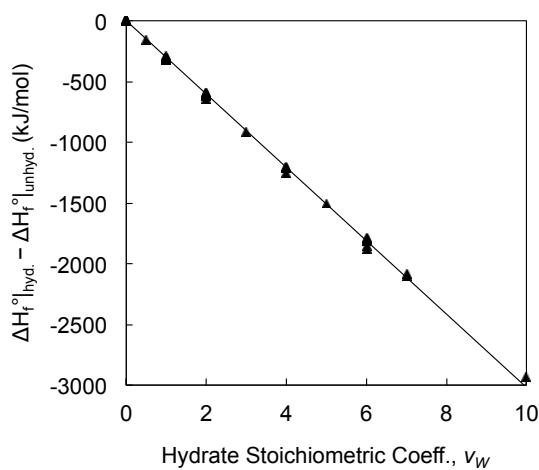
In the case of many hydrated solids, it is difficult to find measurements of the standard state thermodynamic data μ° , $\Delta_f H^\circ$, and C_P° for all hydrated forms. However, the contribution of each additional water molecule to the pure solid appears to be roughly equivalent, as evidenced by the linearity in [Fig. 2](#). The figure shows the difference between the standard state thermodynamic properties of hydrated solids and their unhydrated counterparts versus the stoichiometric coefficient of hydrated water, ν_W . The slope of the best fit lines in [Fig. 2](#) provide estimates of the change in standard state properties as a function of ν_W . Thus, in cases where data on hydrates were incomplete, they were estimated according to $\xi_{\text{MX}\cdot n\text{H}_2\text{O}} = \xi_{\text{MX}} + \nu_W \xi'$, where ξ is any of the three thermodynamic properties (G , H , or C_P). When data on one or more hydrated forms of a single species were available, ξ' was estimated from those data alone; otherwise, ξ' was taken as the relevant slope from [Fig. 2](#). The particular values estimated in this manner are highlighted in [Appendix C](#). Similar methods have been used with success elsewhere, e.g., [\[24, 31\]](#).

3.2.4. Ion Speciation

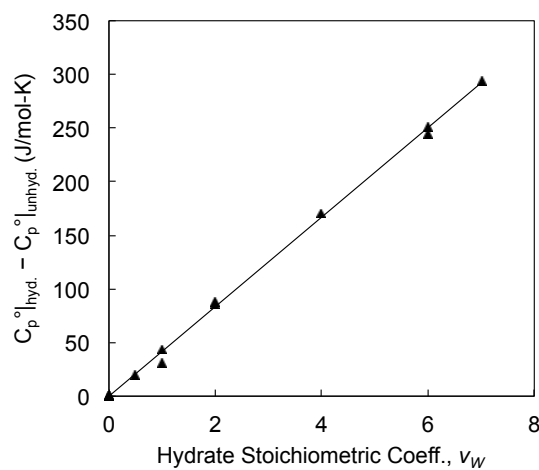
In specific interaction models like Pitzer's, ion association is generally accounted for implicitly, avoiding the additional computation and complexity associated with solving the speciation problem [\[18\]](#). This approach produces results in good agreement with experimental data on many electrolytes that are known to



(a) Gibbs free energy, regressed slope: -244.59 kJ/mol , $R^2 = 0.998$



(b) Enthalpy, regressed slope: -301.85 kJ/mol , $R^2 = 0.999$



(c) Heat capacity, regressed slope: 41.717 J/mol-K , $R^2 = 0.999$

Figure 2: The change in standard state thermodynamic properties as a function of the stoichiometric coefficient of hydrated water

associate, even e.g., in the case of electrolytes such as CuSO_4 , where the tendency to associate is strong [32]. However, in many cases, it has been found that the data are not well represented by the model without the explicit inclusion of a complex species [20, 33, 34]. For this reason, the activity of a limited number of complex species are solved for explicitly.

Harvie et al. [20] and Weare [35] provide guidelines in terms of dissociation constants as to which complexes should be included. For 2-1 electrolytes a dissociation constant of $K \lesssim 0.01$ to 0.05 necessitates the inclusion of the complex; for 2-2 electrolytes the threshold value is $K \lesssim 0.002$. In addition to those mentioned by Harvie et al. [20], we include the following: BaOH^+ , CoOH^+ , FeCO_3^0 , FeHCO_3^+ , FeOH^+ , MnCO_3^0 , MnHCO_3^+ , MnOH^+ , and SrCO_3^0 . Their standard state thermophysical data are tabulated in Appendix C. However, owing to lack of data, the estimation of activity coefficients of these complexes is difficult.

The amount of a constituent in any of these associated forms is computed from equilibrium constants and relevant conservation laws. Free ion and complex activities are computed so that equilibrium constants are satisfied and mass is conserved, and, if necessary, charge is conserved:

$$K = \prod_i a_i^{\nu_i} \quad (14)$$

$$m_T = \sum_i \frac{a_i}{\gamma_i} \quad (15)$$

$$0 = \sum_i m_i z_i \quad (16)$$

3.3. Validation

The model described above is validated using experimental solubility data. Because the model gives SI as a function of pH, temperature, and solute concentration, the solute concentration at saturation (i.e., the solubility) can be calculated by solving for the concentration(s) at which $\text{SI} = 0$ using a non-linear (iterative) solving routine. These solubility predictions are then benchmarked against data for simple single and mixed electrolytes over the temperature range considered here (25–80 °C). As shown and discussed in more detail below, the model predicts solubilities well for a wide variety of compounds, with increasing error at higher temperatures.

Figure 3 shows a comparison of experimental and predicted phase diagrams for a two simple mixed electrolytes (Na-Cl- SO_4 and Na-K-Cl) at 25 °C and 1 bar. The predicted values, represented by solid lines, agree well with the experimental data points indicated by the filled circles. Experimental values were taken from the extensive compilations of Linke and Seidell [36].

In Sec. 3, we discussed the approximations implemented in modeling the temperature dependence of the saturation index: (1) neglecting the temperature dependence of C_P for both solid and aqueous species in the calculation of K_{sp} at elevated temperatures; and (2) neglecting the temperature dependence of the Pitzer parameters, confining the temperature dependence of the activity coefficient to the A^ϕ term. Following the procedure of Pabalan and Pitzer [24], a model for the prediction of SI with full temperature dependence was constructed using curve fits for specific heat as a function of temperature (given by [24, 37, 38]) and curve fits

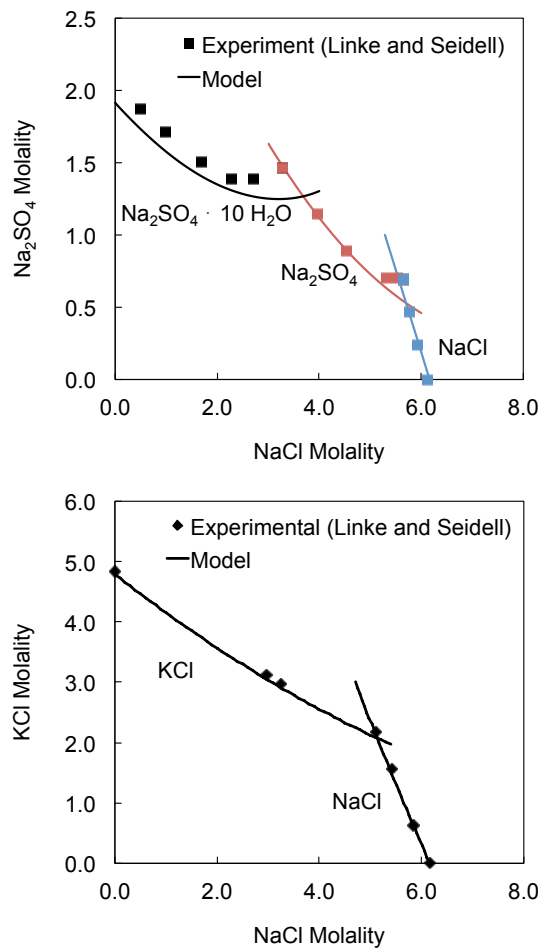
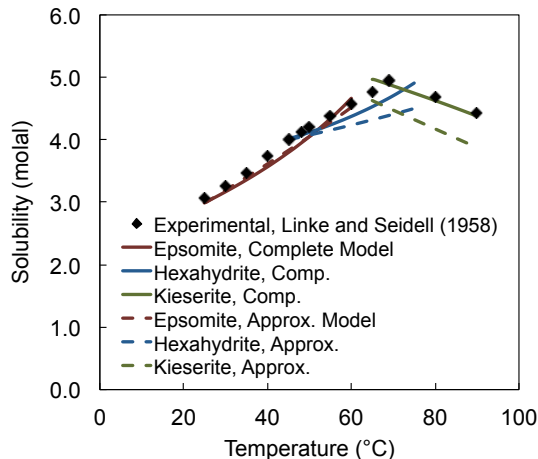
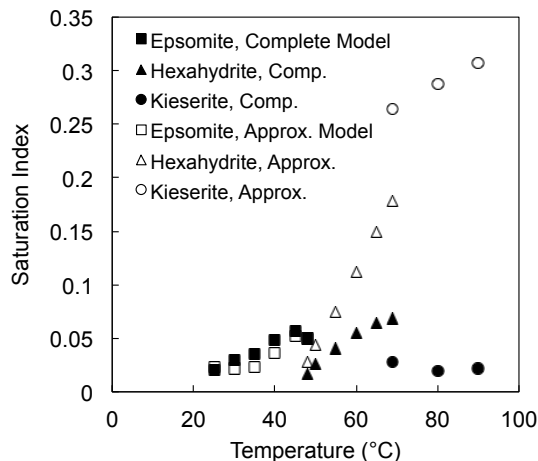


Figure 3: The solubility predictions of the model agree well with experimental data in mixed electrolyte systems at 25 °C and 1 bar



(a) MgSO_4 solubility



(b) MgSO_4 SI at saturation

Figure 4: Comparison of the approximate model with experimental data for the three stable MgSO_4 hydrates (epsomite is the heptahydrate, hexahydrate the hexahydrate, and kieserite is the monohydrate) showing close agreement up to about 60°C

for the Pitzer parameters as a function of temperature [37]. Comparing this model with experimental data and the present (approximate) model allows us to quantify the error associated with our approximations alone. As shown in Fig. 4a, a plot of the MgSO_4 system over $25\text{--}90^\circ\text{C}$, the model absent approximations agrees well with the data over the entire domain; the approximate model is qualitatively satisfactory up to about 50°C , after which the trend is correct, but specific values less so. Figure 4b shows the same comparison in SI-space (in a form similar to the results in Sec. 4): for the approximate model, the absolute error in SI is less than 0.1 up to 60°C , and less than 0.3 for the upper portion of the domain.

Additional confidence in the model is given by the comparisons between predictions and experimental data shown in Fig. 5. Figure 5 compares predictions of SI for NaCl over a range of mostly subsaturated temperature and concentrations to values calculated from data presented by Pitzer et al. [39]. For simple electrolytes like NaCl, it appears that very little accuracy in SI is sacrificed by employing the approximations

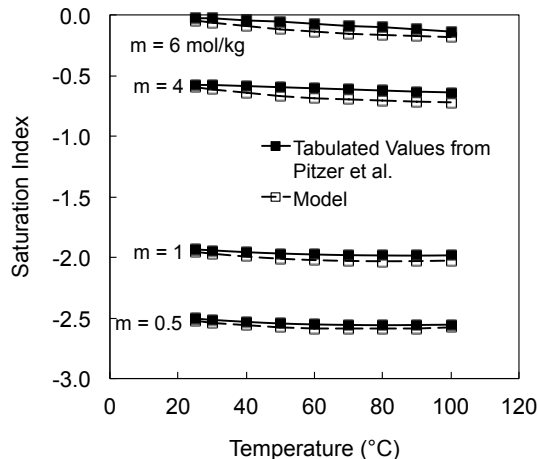


Figure 5: Comparison of the saturation index from the approximate model values calculated from tabulated values in the literature over a wide range of temperature and concentration

in the present model.

4. The Variation of SI with Recovery, Temperature, and pH

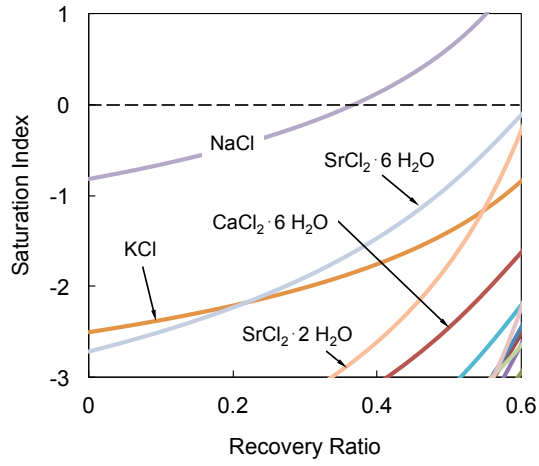
In this section, the analyses of the design-case water samples given in Sec. 2 using the methodology described in Sec. 3 are presented. The variables recovery ratio, temperature, and pH form an operating space. Each subsection contains the effect of a single variable while keeping the other two variables at their nominal values. The effects of these variables on SI are then grouped by anion. Effects over a given process path (in terms of RR, T , and pH) can then be estimated by adding changes in SI as a function of the change in each individual variable. However, some interesting combined effects (e.g., high temperature and high RR) are shown explicitly in the final subsection.

4.1. Effect of Recovery Ratio

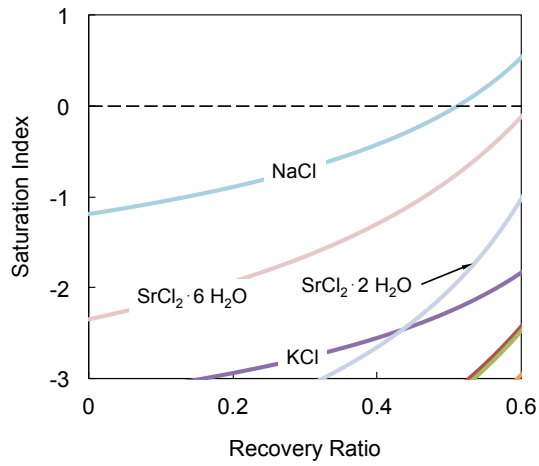
The saturation index as a function of recovery ratio is shown for chloride salts in Fig. 6. Owing to the relatively large fraction of sodium and chloride ions in the produced water makeup, NaCl is the first to reach saturation among the highly-soluble chloride salts. In the Permian sample, this saturation occurs at a recovery ratio of about 37%; in the slightly less saline Marcellus sample it occurs at nearly 50% (Fig. 6). Because the salts in these produced waters are primarily sodium chloride by mass, these values at NaCl saturation are essentially a hard upper limit on recovery ratio.

Strontium chloride nears its solubility limit at around 60% recovery ratio and appears to be unproblematic in the design-case samples. However, a sample with significantly higher strontium concentrations may result in the salt becoming saturated with or before NaCl.

The effects of RR on the SI of the carbonate salts are shown in Fig. 7. The Permian design-case water sample is nearly saturated with several carbonates, and the risk for carbonate scale appears in the Marcellus

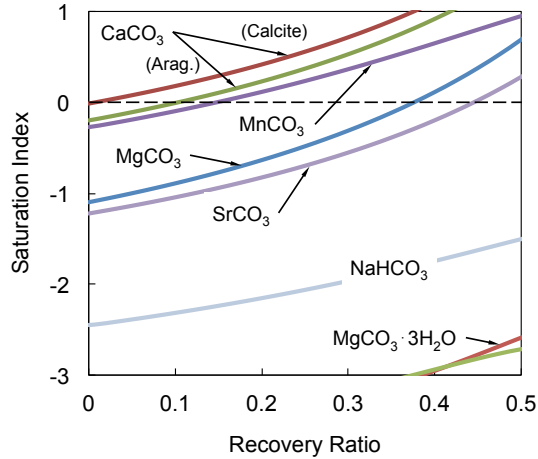


(a) Permian Basin

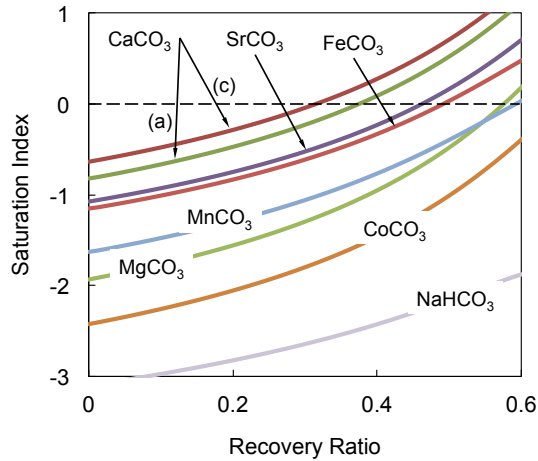


(b) Marcellus

Figure 6: Effect of recovery ratio on the saturation index of chloride salts ($T = 25\text{ }^{\circ}\text{C}$, $\text{pH} = 6$)



(a) Permian Basin



(b) Marcellus

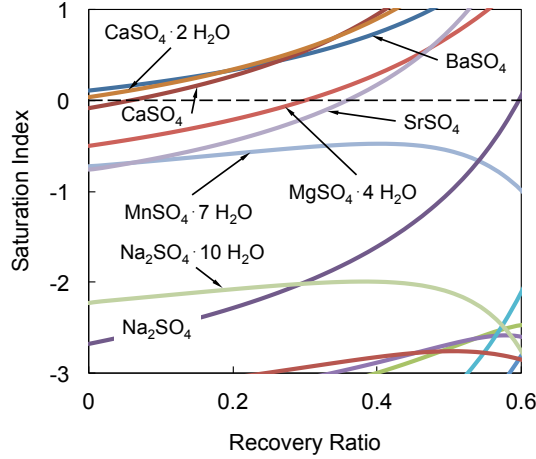
Figure 7: Effect of recovery ratio on the saturation index of carbonate salts ($T = 25\text{ }^\circ\text{C}$, $\text{pH} = 6$)

sample as well. Most significant among them are the prototypical² CaCO_3 , but also FeCO_3 , MgCO_3 , MnCO_3 , and SrCO_3 . In the Permian sample, CaCO_3 , MgCO_3 and MnCO_3 are supersaturated by about 15% recovery, whereas the carbonates appear to remain in solution longer in the Marcellus sample. Cobalt carbonate may be problematic in the Marcellus when Co^{2+} concentrations are significantly higher than the design-case sample. As is typical in the control of CaCO_3 scale in many seawater systems, the scaling potential of these salts can be mitigated through pH control, as discussed in Sec. 4.3, or by the use of antiscalants.

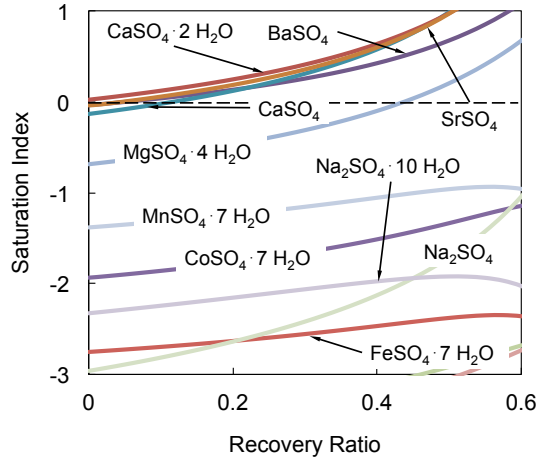
Sulfate scale supersaturation, as shown in Fig. 8, is likely to be the most problematic. Calcium, barium, and strontium sulfates are highly supersaturated almost immediately, and there appears to be a risk for MgSO_4 scaling close to the maximum recovery in both cases³. As a result of high sulfate concentrations and

²The two lines for CaCO_3 correspond to the two polymorphs aragonite and calcite. Although calcite is the more stable polymorph, when both are supersaturated, aragonite may be kinetically preferred under certain conditions [40].

³In most cases, as expected, the saturation index increases at a rising rate as RR becomes greater. In the case of some



(a) Permian Basin



(b) Marcellus

Figure 8: Effect of recovery ratio on the saturation index of sulfate salts ($T = 25\text{ }^\circ\text{C}$, $\text{pH} = 6$)

the presence of extremely sparingly soluble compounds like BaSO_4 , it may be difficult to avoid significant sulfate scale formation. In addition, many of the sulfate compounds display inverse solubility (see Sec. 4.2), meaning precipitation will be increasingly likely in higher temperature (thermal) systems. Some possible mitigation methods will be discussed in Sec. 5.

With values of SI at or well below -5 at recovery ratios less than 50%, bases are unlikely to precipitate at low to moderate pH. This is in contrast to seawater, for which $\text{Mg}(\text{OH})_2$ scaling is a significant issue. The highly-soluble bromide salts also appear to remain completely subsaturated over the given recovery. A potential exception is $\text{NaBr} \cdot 2\text{H}_2\text{O}$, which could reach saturation before NaCl if bromide concentrations

highly hydrated salts (e.g., $\text{MnSO}_4 \cdot 7\text{H}_2\text{O}$ and $\text{Na}_2\text{SO}_4 \cdot 10\text{H}_2\text{O}$ in Fig. 8), however, the saturation index begins to decrease at higher RR. For solutions of high ionic strength, the activity of water may decrease well below its mole fraction. Because the saturation index of hydrated salts is a function of a_W raised ν_W , the SI for highly hydrated compounds can decline at high RR. This behavior is typical of many salts with high propensity towards highly hydrated forms [41]. This behavior should not be seen as an increase in solubility so much as a thermodynamic preference for a different hydrate.

deviated significantly from the design case samples.

Of the three operating variables considered in this analysis, the concentrative effect of recovery ratio on saturation index proves to be the most significant. This results from a two-part, compounding effect on the saturation index as the recovery ratio is increased. First, as more solvent is removed, the concentration of dissolved compounds increases nonlinearly [see Eq. (9)]. In addition, for many electrolytes, the activity coefficients also increase dramatically at high ionic strengths [42]. These two, strong effects appear together as a product in the expression for SI, Eq. (2), and in many cases result in very sharp increases in SI at high RR, with the change in SI differing depending on the compound considered.

Ultimately, this reflects a fundamental physical constraint in the treatment of the considered produced water: high RR is difficult to achieve in untreated water without crystallization. Although this conclusion may seem obvious, it cannot be generalized to all types of produced water, nor even classified using the TDS of a sample alone. For example, based on data from the Maritimes Basin in Nova Scotia, Thiel et al. [43] have given theoretical evidence to show that produced water having nearly twice the concentration of seawater may be treated to 70–80% recovery without any likely precipitation and very minimal pretreatment. The upper bound on recovery ratio, as defined here in thermodynamic terms, is thus fundamentally dependent on the details of any given produced water composition.

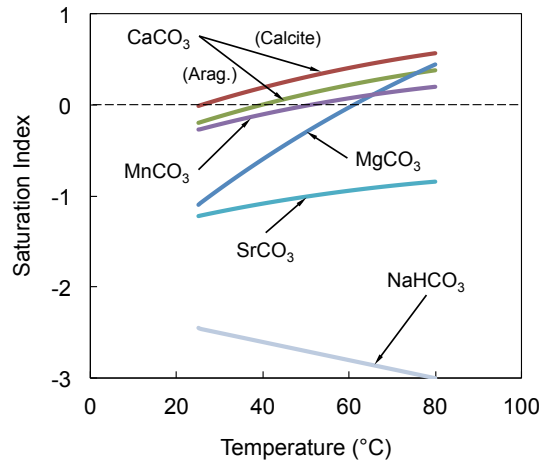
4.2. Effect of Temperature

The effect of temperature on saturation index is generally the most difficult to capture. As outlined in Sec. 3, in principle all of the quantities in the saturation index are complex, nonlinear functions of temperature. As a result, the temperature domain analyzed here has been limited to 25–80 °C, which is generally within the space of both many thermal desalination systems and the established limits of the model itself.

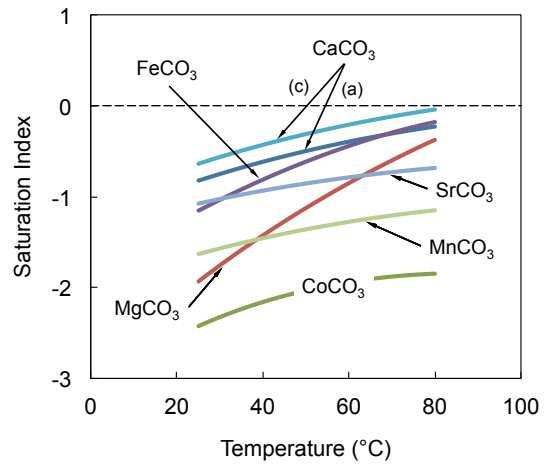
The effects of temperature on carbonate salt saturation indices are shown in Fig. 9. The characteristic inverse solubility behavior of calcium carbonate is reflected in the positive slope of its SI; even a modest increase in temperature at zero recovery may encourage its precipitation in the Permian sample. The salts CoCO_3 , FeCO_3 , MgCO_3 , MnCO_3 , and SrCO_3 also display inverse solubility. In particular, the inverse solubility behavior of CoCO_3 may encouraged formation at high temperatures because it is only slightly subsaturated at higher RR and 25 °C (cf. Fig. 7b).

The temperature dependence of sulfate scale saturation indices are shown in Fig. 10. The relatively shallow slope of the line corresponding to calcium sulfate dihydrate (gypsum) displays behavior similar to measurements of solubility in pure water. The anhydrous form (anhydrite) becomes more supersaturated at higher temperatures. Barium and strontium sulfate appear to be the only scales that are close to their saturation limits and also benefit significantly from increased temperature.

For chloride salts nearest their saturation limits, namely NaCl , KCl , and $\text{SrCl}_2 \cdot 6\text{H}_2\text{O}$, the saturation index decreases modestly as temperature increases, reflecting the expected normal solubility behavior of these salts. The relatively small sensitivity of SI to temperature in most chloride salts near saturation means

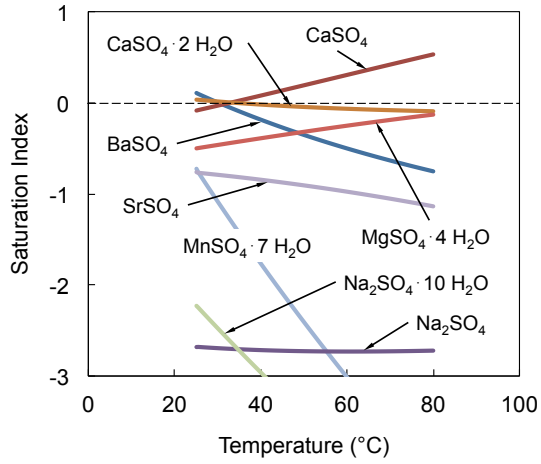


(a) Permian Basin

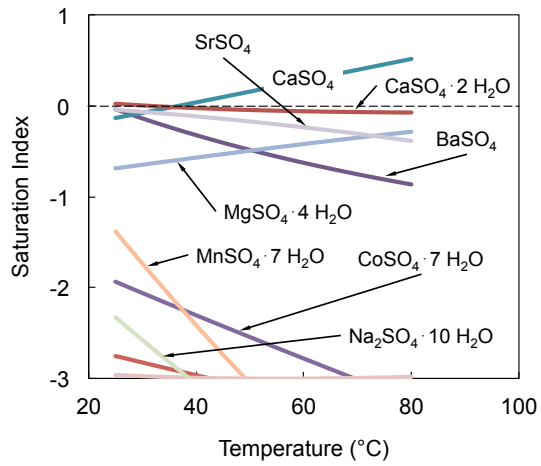


(b) Marcellus

Figure 9: Effect of temperature on the saturation index of carbonate salts (RR = 0, pH = 6)



(a) Permian Basin



(b) Marcellus

Figure 10: Effect of temperature on the saturation index of sulfate salts (RR = 0, pH = 6)

that, in general, the temperature range of a chosen treatment system is unlikely to have major effects on the crystallization potential of chloride salts.

The effect of temperature on SI is strong on the bases: all demonstrate significant inverted solubility, with many undergoing a change in SI of 3–4 over a 55 K temperature change. Nevertheless, despite their relevance as seawater scales, as discussed in Sec. 4.1, most bases in the present water, including $\text{Mg}(\text{OH})_2$, appear sufficiently below $\text{SI} = 0$ to be unproblematic at low pH.

4.3. Effect of pH

Owing to acid/base equilibria and the tendency for certain electrolytes, particularly 2-2 electrolytes and transition metals, to associate, the saturation indices of carbonate and hydroxide all show significant pH dependence. As shown in Fig. 11a, calcium carbonate appears likely to scale in both samples, with its SI reaching zero at a pH of about 6 at zero recovery. The relatively significant quantities of iron, magnesium, manganese, and strontium ions in the produced water mean that both manganese and strontium carbonate are likely to crystallize along with calcium carbonate at similar values of pH. Cobalt carbonate is somewhat undersaturated near values of pH between 4 and 7, but may become scale forming at high recovery ratios as their concentrations are increased.

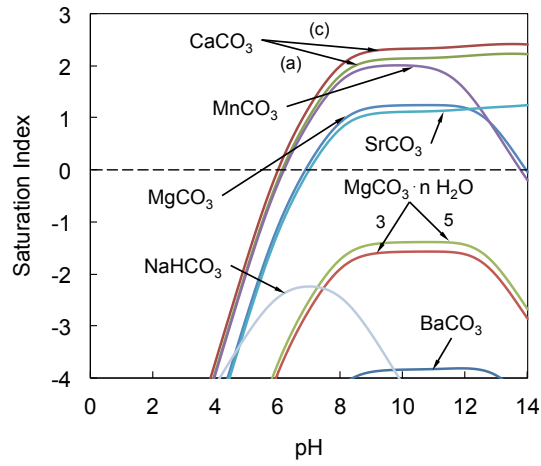
The saturation indices of carbonate salts closely mirror the pure carbonate equilibrium. As the pH decreases below values around 6, the concentration of free carbonate ions, CO_3^{2-} drops sharply, resulting in a decline in the SI of CaCO_3 , FeCO_3 , MgCO_3 , MnCO_3 , and SrCO_3 . Likewise, NaHCO_3 reaches its maximum in SI around neutral values of pH, where the dissolved carbon exists mostly as HCO_3^- . The decrease in SI seen at higher pH results from significant metal hydrolysis and/or metal-(bi)carbonate ion pairing. This ion pairing at the higher pH reduces the free metal activity, and thus the SI of the metal-carbonate salts.

The effect of pH on the saturation index of hydroxide compounds is shown in Figure 12. As expected, the saturation index displays a predominantly linear trend owing to the water self ionization equilibrium. At very high values of pH, however, the saturation indices of $\text{Co}(\text{OH})_2$, $\text{Fe}(\text{OH})_2$, and $\text{Mn}(\text{OH})_2$ show nonlinear behavior as a result of increased concentrations of metal-OH complexes, reducing the rate at which SI increases with increasing pH. Of the bases presented, $\text{Co}(\text{OH})_2$, $\text{Fe}(\text{OH})_2$, $\text{Mg}(\text{OH})_2$ and $\text{Mn}(\text{OH})_2$ appear closest to saturation. Unlike seawater, however, they appear unlikely to form scale in the absence of very high recovery ratios, or very basic pH.

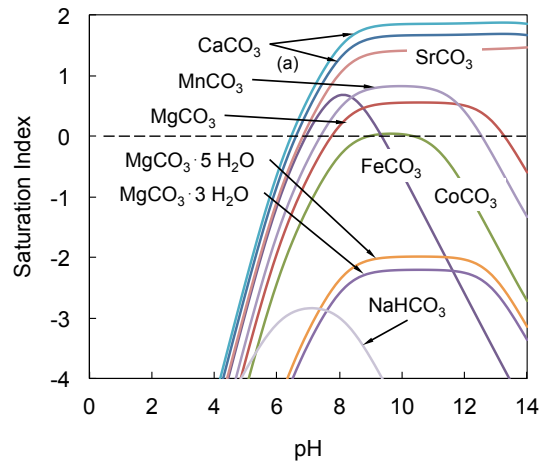
4.4. Combined Effects

Temperature, recovery ratio and pH define the domain for the SI of the compounds considered here. We have attempted to show this SI space by varying each of these variables individually and independently. However, depending on the process path in the desalination system, all three variables may change simultaneously. In this section, we highlight some cases where these changes are of interest.

Because sodium chloride has normal solubility behavior, (i.e., increasing solubility with increasing temperature) the maximum recovery ratio can be increased slightly at higher temperature. This behavior is shown

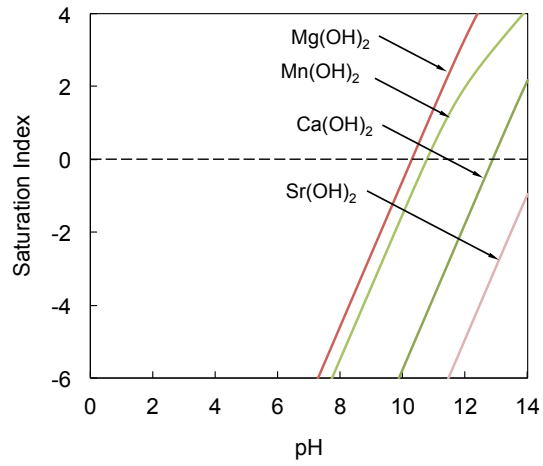


(a) Permian Basin

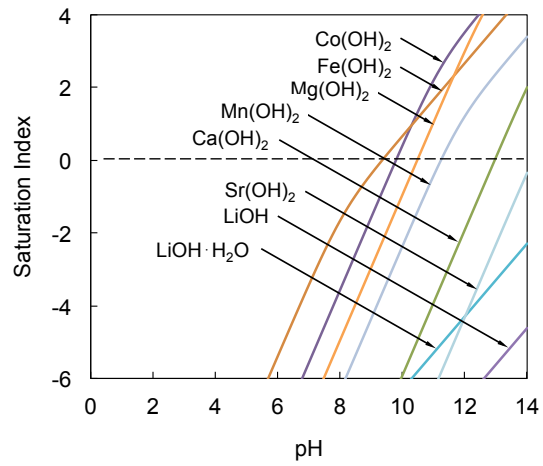


(b) Marcellus

Figure 11: Effect of pH on the saturation index of carbonate salts (RR = 0, T = 25 °C)



(a) Permian Basin



(b) Marcellus

Figure 12: Effect of pH on the saturation index of bases (RR = 0, $T = 25^\circ C$)

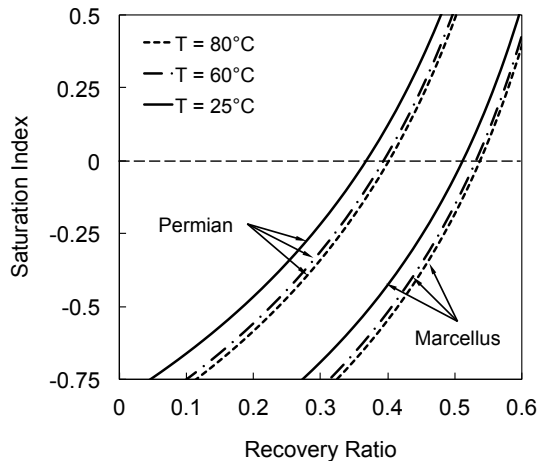


Figure 13: SI of NaCl versus recovery ratio at 25 °C, 60 °C, and 80 °C

in Figure 13, where the maximum RR increases by about 4% by increasing the temperature from 25 °C to 80 °C. Of course, however, as the waste brine cools after it is discharged, it will become supersaturated with respect to NaCl, creating a risk for NaCl crystallization.

As seen in Figure 14, which shows SI versus pH for selected carbonate salts at maximum recovery (as defined by NaCl saturation) and $T = 80\text{ °C}$, the SI curves essentially shift upward by the net changes in SI shown in Figs. 7 and 9. The apparent differences in shape between the curves in Fig. 14 and 11a at high pH result from increased ion-pairing at the higher metal concentrations. Thus, for thermal systems operating near 80 °C, the optimum pretreatment for carbonate salts is one which reduces the outlet pH to the value at which SI for CaCO_3 (the carbonate salt with the highest scaling propensity in both samples), is zero. In the case of the Permian, the desired pH is about 5; in the Marcellus sample it is about 5.2.

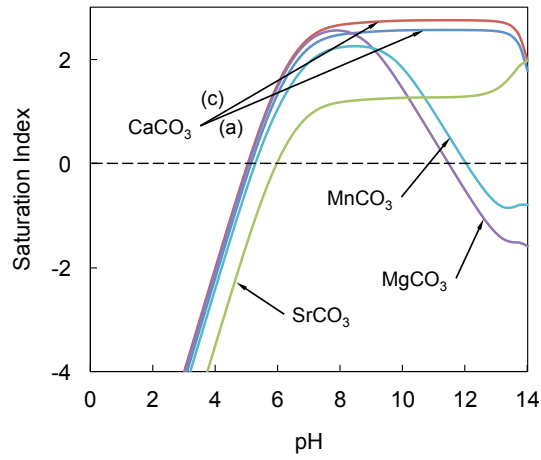
Likewise, as seen in Fig. 15, the risk of basic scale formation is strongly affected by both pH and temperature. Comparing Fig. 15 to Fig. 12, we see that the curves at low temperature and zero recovery have shifted upwards significantly—with saturation indices increasing by about 3 to 4 in many cases. This is primarily a result of strong inverted solubility behavior common to these compounds. Nevertheless, as long as pH remains below about 8.5 in the Permian or 8.2 in the Marcellus, basic scale formation appears unlikely.

5. Impacts on System Design and Selection

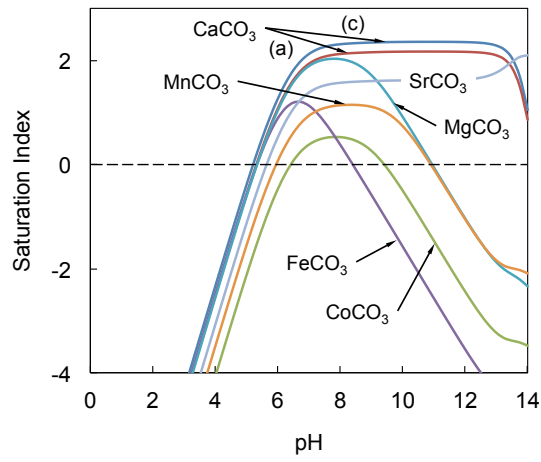
The influence of water composition on system operating conditions is now considered. The results from Sec. 4 are synthesized into an operating envelope defined by solid-liquid equilibrium, with brief discussion on the limitations of this system-unspecific approach. The section concludes with remarks on potential mitigation methods for scales that may be unavoidable through thermodynamic design considerations alone.

5.1. The Scale-Defined Operating Envelope

By synthesizing the effects studied individually in Sec. 4, a set of operating conditions in terms of temperature, pH, and recovery ratio can be identified. Figure 16 shows the SI of compounds nearest to

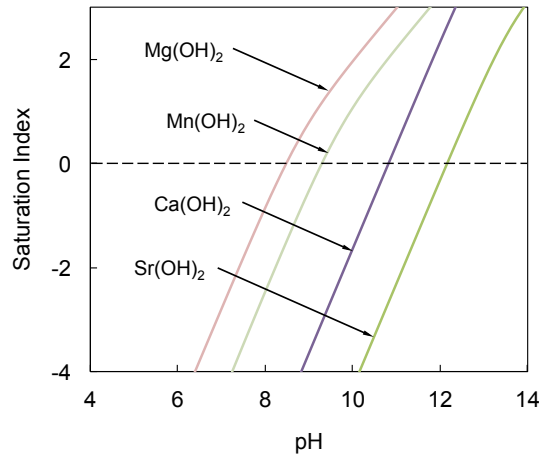


(a) Permian Basin

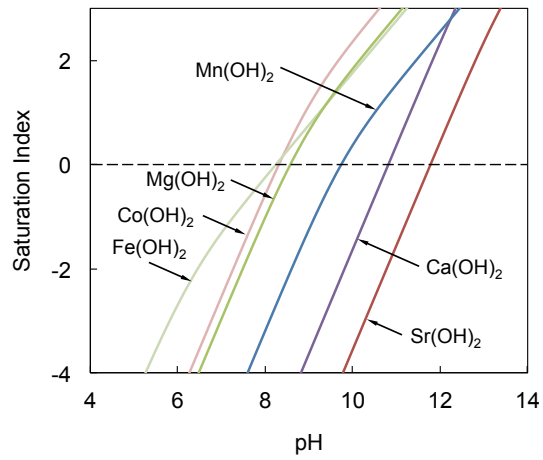


(b) Marcellus

Figure 14: Effect of pH on the saturation index of carbonates at high temperature and RR ($RR = RR_{max}$, $T = 80^\circ C$)

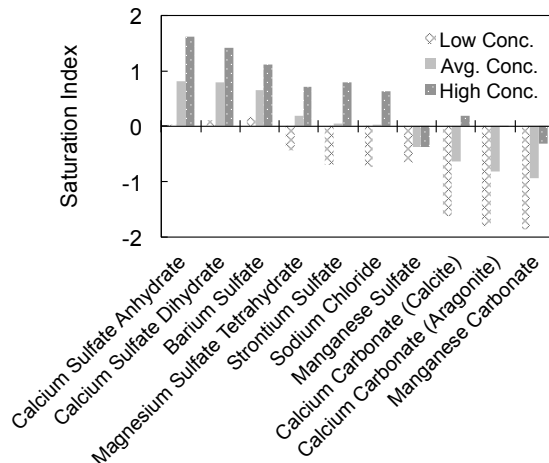


(a) Permian Basin

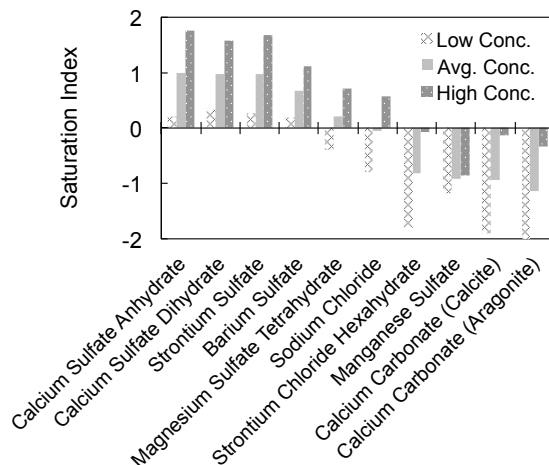


(b) Marcellus

Figure 15: Effect of pH on the saturation index of bases at high temperature and RR ($RR = RR_{max}$, $T = 80^\circ C$)



(a) Permian, RR = 0.37, pH = 5, $T = 25^\circ\text{C}$



(b) Marcellus, RR = 0.5, pH = 5, $T = 25^\circ\text{C}$

Figure 16: The operating envelope defined by solid-liquid equilibrium: NaCl sets an upper bound on recovery ratio, but moderate pH adjustment can reduce the likelihood of crystallization of all but a handful of compounds.

saturation ($SI > -2$) at these conditions. In order to account for variability in water composition, three different sample make-ups are shown in the figures. The values shown in Table 2 have been perturbed by $\pm 40\%$ to estimate representative high and low concentration samples; the bars marked as average correspond to the composition in Table 2. In the case of the average Permian sample, a reduction in pH to 5 allows for a recovery ratio of 37% to be reached with only four salts showing supersaturated conditions: BaSO_4 , CaSO_4 , MgSO_4 , and SrSO_4 . The Marcellus sample displays similar results with pH adjustment, but higher recovery ratios are achieved owing to lower NaCl concentrations in the average case.

As a result of the high concentrations of sulfates, it seems it is difficult to design operating conditions around the formation of BaSO_4 , CaSO_4 , MgSO_4 , and SrSO_4 . Because SrSO_4 and BaSO_4 are so sparingly soluble, however, a measure of supersaturation may be tolerable for some time before a significantly sized deposit builds up. In addition, because the major impacts of temperature variation on SI values near

saturation are confined to the sulfates, it appears that scale formation does not place a clear bound on operating temperature. That is, at higher temperatures, the formation of BaSO_4 and SrSO_4 is less favored, but the formation of CaSO_4 is more favored.

In addition, of course, local conditions in desalination systems may differ considerably from the nominal ‘bulk’ values discussed thus far. Increases in temperature near a heat transfer surface, concentration polarization near a liquid-membrane interface, and chemical interactions between the water and system hardware may all favor local solid formation (see, e.g., [44]) despite a nominally subsaturated condition in a mass-averaged sense. These effects may place additional constraints on system operating conditions.

We also have not considered the effects of pressure. The effect of pressure on the solubility product tends to be small. However, when vapor-liquid equilibrium is considered—as in the case of evaporative desalination technologies—significant quantities of dissolved gases can escape the solution and effect solid formation. An important example of this phenomenon is the release of CO_2 as the pressure is reduced in multi-effect evaporation and multi-stage flash desalination, which can cause an increase in pH and the formation of CaCO_3 scale [45].

5.2. Options for mitigation

Several methods are available to reduce the potential for BaSO_4 , CaSO_4 , MgSO_4 , and SrSO_4 formation. Perhaps the most common option is chemical softening, which would precipitate the barium, calcium, magnesium, and strontium (and other compounds) as metal-carbonate salts. Nanofiltration has also been used to remove divalent ions [46] in a pretreatment step. Antiscalants, such as any number of EDTA salts, can complex scale-forming metals, effectively reducing the activity of the free metal ion. Finally, there is ongoing research into surface modification to prevent or slow the nucleation of solids onto vital heat transfer or membrane surfaces (see, e.g., [47]).

6. Conclusions

In produced water treatment, the fundamental goal is efficient waste concentration. With hypersaline feed water, solids formation in high-recovery desalination systems is inevitable. In this work, original data describing the composition of produced water from hydraulic fracturing in the Permian Basin and the Marcellus have been presented and analyzed from the standpoint of treatment. The following conclusions were demonstrated:

1. In the absence of pretreatment, the most likely scales, as determined by highest saturation indices are: calcium carbonate, iron carbonate, magnesium carbonate, manganese carbonate, strontium carbonate, barium sulfate, calcium sulfate, magnesium sulfate, and strontium sulfate.
2. As in seawater desalination systems, pH control appears highly effective in the mitigation of carbonate scale, allowing recovery ratios of about 40–50% to be achieved without encouraging carbonate salt precipitation.

3. Most compounds do not have saturation indices sufficiently and uniformly sensitive enough to temperature to allow temperature-mediated scale control. BaSO_4 and SrSO_4 may be exceptions, as their saturation indices changes by about 1 and 0.5, respectively, over the temperature domain examined here. All the carbonate scales mentioned in item (1) display inverted solubility over the examined temperature domain, indicating a greater risk for scale at higher temperatures. Calcium and magnesium sulfate also display inverted solubility.
4. Of the three physical effects analyzed (temperature, pH, and recovery ratio), recovery ratio has the strongest influence on the saturation index owing to the removal of solvent and often increasing activity coefficients at higher ionic strength. Ultimately, with pH adjustment and some measure to control barium, calcium, magnesium, and strontium sulfate scale formation, recovery ratios of about 40–50% can be reached in conventional desalination systems capable of handling high salinity waters.

Acknowledgements

The authors would like to thank the King Fahd University of Petroleum and Minerals for funding the research reported in this paper through the Center for Clean Water and Clean Energy at MIT and KFUPM under project number R4-CW-08. The first author would also like to extend his gratitude to the MIT Energy Initiative and the Martin Family Foundation for fellowship support.

- [1] U. S. Energy Information Agency, “Annual Energy Outlook 2013,” 2013.
- [2] U. S. Energy Information Administration, “Technically Recoverable Shale Oil and Shale Gas Resources: An Assessment of 137 Shale Formations in 41 Countries Outside the United States,” June 2013.
- [3] U. S. Environmental Protection Agency, “Natural Gas — Clean Energy — US EPA.” <<http://www.epa.gov/cleanenergy/energy-and-you/affect/natural-gas.html> >.
- [4] U. S. Department of Energy and the National Energy Technology Laboratory, “Modern Shale Gas Development in the United States: A Primer,” 2009.
- [5] S. A. Holditch, “Getting the gas out of the ground,” *Chemical Engineering Progress*, vol. 108, pp. 41–48, August 2012.
- [6] “Produced water pretreatment for water recovery and salt production,” Tech. Rep. 08122-36, Research Partnership to Secure Energy for America, 2012.
- [7] M. Bomgardner, “Treating water from hydraulic fracturing,” *Chemical & Engineering News*, vol. 90, pp. 13–16, October 2012.
- [8] C. E. Clark and J. A. Veil, “Produced Water Volumes and Management Practices in the United States,” September 2009.
- [9] W. L. Ellsworth, “Injection-induced earthquakes,” *Science*, vol. 341, pp. 142–149, July 2013.
- [10] S. Horton, “Disposal of hydrofracking waste fluid by injection into subsurface aquifers triggers earthquake swarm in central Arkansas with potential for damaging earthquake,” *Seismological Research Letters*, vol. 83, pp. 250–260, March/April 2012.
- [11] Ohio Department of Natural Resources, “Preliminary Report on the Northstar 1 Class II Injection Well and the Seismic Events in the Youngstown, Ohio Area,” tech. rep., 2012.
- [12] K. M. Keranen, H. M. Savage, G. A. Abers, and E. S. Cochran, “Potentially induced earthquakes in Oklahoma, USA: Links between wastewater injection and the 2011 M_w 5.7 earthquake sequence,” *Geology*, 2013.
- [13] A. Marshall, “New wave of injection wells on the way in Ohio for fracking waste,” *The Plain Dealer*, November 2012.
- [14] S. Rassenfoss, “From Flowback to Fracturing: Water Recycling Grows in the Marcellus Shale,” *Journal of Petroleum Technology*, vol. 63, no. 7, pp. 48–51, 2011.
- [15] R. Y. Ning, “Discussion of silica speciation, fouling, control and maximum reduction,” *Desalination*, vol. 151, pp. 67–73, 2002.

- [16] W. Stumm and J. J. Morgan, *Aquatic Chemistry: Chemical Equilibria and Rates in Natural Waters*. John Wiley & Sons, 3rd ed., 1996.
- [17] K. S. Pitzer and J. J. Kim, “Thermodynamics of Electrolytes. IV. Activity and Osmotic Coefficients for Mixed Electrolytes,” *Journal of the American Chemical Society*, vol. 96, pp. 5701–5707, September 1974.
- [18] K. S. Pitzer, “A thermodynamic model for aqueous solutions of liquid-like density,” *Reviews in Mineralogy and Geochemistry*, vol. 17, pp. 97–142, 1987.
- [19] C. E. Harvie and J. H. Weare, “The prediction of mineral solubilities in natural waters: the Na-K-Mg-Ca-Cl-SO₄-H₂O system from zero to high concentration at 25 °C,” *Geochimica et Cosmochimica Acta*, vol. 44, pp. 981–997, 1980.
- [20] C. E. Harvie, N. Mller, and J. H. Weare, “The prediction of mineral solubilities in natural waters: The Na-K-Mg-Ca-H-Cl-SO₄-OH-HCO₃-CO₃-CO₂-H₂O system to high ionic strengths at 25 °C,” *Geochimica et Cosmochimica Acta*, vol. 48, pp. 723–751, 1984.
- [21] K. S. Pitzer, “Thermodynamics of Electrolytes. I. Theoretical Basis and General Equations,” *Journal of Physical Chemistry*, vol. 77, no. 2, pp. 268–277, 1973.
- [22] J. F. Zemaitis, D. M. Clark, M. Rafal, and N. C. Scrivner, *Handbook of Aqueous Electrolyte Thermodynamics*. Wiley-AIChE, 1986.
- [23] K. H. Mistry, H. A. Hunter, and J. H. Lienhard V, “Effect of composition and nonideal solution behavior on desalination calculations for mixed electrolyte solutions with comparison to seawater,” *Desalination*, vol. 318, pp. 34–47, 2013.
- [24] R. T. Pabalan and K. S. Pitzer, “Thermodynamics of concentrated electrolyte mixtures and the prediction of mineral solubilities to high temperatures for mixtures in the system Na-K-Mg-Cl-SO₄-OH-H₂O,” *Geochimica et Cosmochimica Acta*, vol. 51, pp. 2429–2443, 1987.
- [25] H.-T. Kim and W. J. Frederick, “Evaluation of Pitzer Ion Interaction Parameters of Aqueous Electrolyte Solutions at 25 °C. 2. Ternary Mixing Parameters,” *Journal of Chemical Engineering Data*, vol. 33, pp. 278–283, 1988.
- [26] F. J. Millero and D. Pierrot, “A chemical equilibrium model for natural waters,” *Aquatic Geochemistry*, vol. 4, pp. 153–199, 1998.
- [27] L. F. Silvester and K. S. Pitzer, “Thermodynamics of Electrolytes X. Enthalpy and the effect of Temperature on the Activity Coefficients,” *Journal of Solution Chemistry*, vol. 7, no. 5, pp. 327–337, 1978.

- [28] L. F. Silvester and K. S. Pitzer, “Thermodynamics of Electrolytes. 8. High-Temperature Properties, Including Enthalpy and Heat Capacity, with Application to Sodium Chloride,” *The Journal of Physical Chemistry*, vol. 81, no. 19, pp. 1822–1828, 1977.
- [29] M. P. de Lima and K. S. Pitzer, “Thermodynamics of saturated electrolyte mixtures of NaCl with Na₂SO₄ and with MgCl₂,” *Journal of Solution Chemistry*, vol. 12, no. 3, pp. 187–199, 1983.
- [30] W. M. Haynes, ed., *CRC Handbook of Chemistry and Physics*. CRC Press, 93rd ed., 2012.
- [31] B. S. Hemingway, R. R. Seal II, and I. Chou, “Thermodynamic data for modeling acid mine drainage problems: compilation and estimation of data for selected soluble iron-sulfate minerals,” Open-file report 02-161, U. S. Geological Survey, 2002.
- [32] P. M. May, D. Rowland, G. Hefter, and E. Königsberger, “A generic and updatable pitzer characterization of aqueous binary electrolyte solutions at 1 bar and 25 °C,” *Journal of Chemical and Engineering Data*, vol. 56, pp. 5066–5077, 2011.
- [33] K. S. Pitzer and L. F. Silvester, “Thermodynamics of Electrolytes. VI. Weak Electrolytes Including H₃PO₄,” *Journal of Solution Chemistry*, vol. 5, pp. 269–278, 1976.
- [34] K. S. Pitzer, R. N. Roy, and L. F. Silvester, “Thermodynamics of Electrolytes. 7. Sulfuric Acid,” *Journal of the American Chemical Society*, vol. 99, no. 15, pp. 4930–4936, 1977.
- [35] J. H. Weare, “Models of mineral solubility in concentrated brines with application to field observations,” *Reviews in Mineralogy*, vol. 17, pp. 143–176, 1987.
- [36] W. F. Linke and A. Seidell, *Solubilities: Inorganic and Metal-Organic Compounds*, vol. II. American Chemical Society, 4 ed., 1958.
- [37] R. C. Phutela and K. S. Pitzer, “Heat capacity and other thermodynamic properties of aqueous magnesium sulfate to 473 K,” *Journal of Physical Chemistry*, vol. 90, pp. 895–901, 1986.
- [38] D. G. Archer and J. A. Rard, “Isopiestic investigation of the osmotic and activity coefficients of aqueous mgso₄ and the solubility of MgSO₄ · 7 H₂O(cr) at 298.15 K: thermodynamic properties of the MgSO₄ + H₂O system to 440 K,” *Journal of Chemical Engineering Data*, vol. 43, pp. 791–806, 1998.
- [39] K. S. Pitzer, J. C. Peiper, and R. H. Busey, “Thermodynamic properties of aqueous sodium chloride solutions,” *Journal of Physical and Chemical Reference Data*, vol. 13, pp. 1–102, 1984.
- [40] R. A. Berner, “The role of magnesium in the crystal growth of calcite and aragonite from sea water,” *Geochimica et Cosmochimica Acta*, vol. 39, pp. 489–504, 1975.
- [41] A. S. Myerson, ed., *Handbook of Industrial Crystallization*. Butterworth-Heinemann, 2nd ed., 2002.

- [42] R. A. Robinson and R. H. Stokes, *Electrolyte Solutions*. Dover, 2nd revised ed., 2002.
- [43] G. P. Thiel, S. M. Zubair, and J. H. Lienhard V, “An analysis of likely scalants in the treatment of produced water from Nova Scotia,” *Heat Transfer Engineering*, 2014. Accepted for publication.
- [44] H. Glade, K. Krömer, S. Will, K. Loisel, S. Nied, J. Detering, and A. Kempter, “Scale formation and mitigation of mixed salts in horizontal tube falling film evaporator for seawater desalination,” in *Proceedings of the 10th International Conference on Heat Exchanger Fouling and Cleaning*, (Budapest), pp. 386–396, 2013.
- [45] A. Al-Rawajfeh, H. Glade, and J. Ulrich, “Scaling in multiple-effect distillers: the role of CO₂ release,” *Desalination*, vol. 182, pp. 205–219, 2005.
- [46] N. Hilal, H. Al-Zoubi, N. A. Darwish, A. W. Mohammad, and M. A. Arabi, “A comprehensive review of nanofiltration membranes: Treatment, pretreatment, modelling, and atomic force microscopy,” *Desalination*, vol. 170, pp. 281–308, 2004.
- [47] M. R. Malayeri, A. Al-Janabi, and H. Müller-Steinhagen, “Application of nano-modified surfaces for fouling mitigation,” *International Journal of Energy Research*, vol. 33, pp. 1101–1113, 2009.
- [48] P. Debye and E. Hückel, “Zur theorie der elektrolyte,” *Physikalische Zeitschrift*, vol. 24, pp. 185–206, May 1923.
- [49] M. Uematsu and E. U. Franck, “Static dielectric constant of water and steam,” *Journal of Physical and Chemical Reference Data*, vol. 9, no. 4, pp. 1291–1306, 1980.
- [50] Knovel, “Knovel Critical Tables,” 2008.
- [51] R. A. Robie, B. S. Hemingway, and J. R. Fisher, “Thermodynamic properties of minerals and related substances at 298.15 K and 1 bar pressure and at higher temperatures,” 1978. U.S. Geological Survey Bulletin 1452.
- [52] G. M. Anderson and D. A. Crerar, *Thermodynamics in Geochemistry: The Equilibrium Model*. Oxford University Press, 1993.
- [53] F. M. Morel and J. G. Hering, *Principles and Applications of Aquatic Chemistry*. John Wiley & Sons, 1993.
- [54] D. D. Wagman, W. H. Evans, V. B. Parker, R. H. Schumm, I. Halow, S. M. Bailey, K. L. Churney, and R. L. Nuttall, “The NBS tables of chemical thermodynamic properties: Selected values for inorganic and C₁ and C₂ organic substances in SI units,” *Journal of Physical and Chemical Reference Data*, vol. 11, 1982.
- [55] P. Patnaik, *Handbook of Inorganic Chemicals*. McGraw-Hill, 2002.

- [56] E. L. Shock and H. C. Helgeson, "Calculation of the thermodynamic and transport properties of aqueous species at high pressures and temperatures: Correlation algorithms for ionic species and equation of state prediction to 5 kb and 1000 °C," *Geochimica et Cosmochimica Acta*, vol. 52, pp. 2009–2036, 1988.
- [57] E. L. Shock, D. C. Sassani, M. Willis, and D. A. Sverjensky, "Inorganic species in geologic fluids: Correlations among standard molal thermodynamic properties of aqueous ions and hydroxide complexes," *Geochimica et Cosmochimica Acta*, vol. 61, no. 5, pp. 907–950, 1997.
- [58] D. A. Sverjensky, E. L. Shock, and H. C. Helgeson, "Prediction of the thermodynamic properties of aqueous metal complexes to 1000 °C and 5 kb," *Geochimica et Cosmochimica Acta*, vol. 61, no. 7, pp. 1359–1412, 1997.
- [59] E. L. Shock, H. C. Helgeson, and D. A. Sverjensky, "Calculation of the thermodynamic and transport properties of aqueous species at high pressures and temperatures: Standard partial molal properties of inorganic neutral species," *Geochimica et Cosmochimica Acta*, vol. 53, pp. 2157–2183, 1989.

Appendix A. Derivation of the saturation index

Consider the equilibrium of a pure, solid salt MX and its constituent ions in solution:



At this saturated, equilibrium state, for constant temperature and pressure,

$$dG = \sum_i \mu_i dN_i = (\mu_{MX} - \nu_M \mu_M - \nu_X \mu_X) dN_{MX} = 0 \quad (\text{A.2})$$

where for each species i , μ_i is the chemical potential, defined as

$$\mu_i = \mu_i^\circ + RT \ln a_i \quad (\text{A.3})$$

where a_i is the activity, R is the (universal) gas constant, and T is absolute temperature. Expanding Eq. (A.2) using Eq. (A.3), we find the solubility product, K_{sp} :

$$0 = -\mu_{MX}^\circ + \nu_M \mu_M^\circ + \nu_X \mu_X^\circ + RT \ln \left(\frac{a_M^{\nu_M} a_X^{\nu_X}}{a_{MX}} \right) \quad (\text{A.4})$$

$$= \Delta_r G^\circ + RT \ln K_{sp} \quad (\text{A.5})$$

$$\ln K_{sp} = -\frac{\Delta_r G^\circ}{RT} \quad (\text{A.6})$$

Using similar reasoning, it can be shown that outside of equilibrium, the right hand side of Eq. (A.4) is identically equal to dG/dN_{MX} :

$$\begin{aligned} \frac{dG}{dN_{MX}} &= \Delta_r G^\circ + RT \ln Q = RT \ln \left(\frac{Q}{K_{sp}} \right) \\ &= RT \ln \left(\frac{\prod_i a_i^{\nu_i}}{\prod_i a_{i,\text{sat}}^{\nu_i}} \right) \end{aligned} \quad (\text{A.7})$$

where Q is the activity product. In this way, when $dG = 0$, the definition of the solubility equilibrium, $Q = K_{sp}$. Likewise, the degree to which a solution is supersaturated, in terms of Gibbs free energy, is related to the degree to which Q exceeds K_{sp} . For convenience, the natural log is replaced by a base-10 log, and the saturation index is defined as

$$\text{SI} = \log \left(\frac{Q}{K_{sp}} \right) = \log \left(\frac{a_M^{\nu_M} a_X^{\nu_X} a_W^{\nu_W}}{K_{sp}} \right) \quad (\text{A.8})$$

where the activity of water a_W has been incorporated to reflect the more general case of a hydrated compound.

Appendix B. Pitzer Equations

The term F is based on an extended Debye-Hückel function [48], reflecting the characteristic first-order-square-root dependence on ionic strength caused by long-range electrostatic interactions:

$$\begin{aligned} F &= -A^\phi \left(\frac{\sqrt{I}}{1 + 1.2\sqrt{I}} + \frac{2}{1.2} \ln(1 + 1.2\sqrt{I}) \right) \\ &\quad + \sum_c \sum_a m_c m_a B'_{ca} + \sum_{c < c'} \sum m_c m_{c'} \Phi'_{cc'} \\ &\quad + \sum_a \sum_{a' < a} m_a m_{a'} \Phi'_{aa'} \end{aligned} \quad (\text{B.1})$$

The parameter A^ϕ is related to the Debye-Hückel limiting law, and is given by

$$A^\phi = \frac{1}{3} \sqrt{\frac{2\pi N_A \rho_s}{1000}} \left(\frac{e^2}{\varepsilon k_B T} \right)^{3/2} \quad (\text{B.2})$$

where N_A is Avogadro's number, ρ_s is the density of the pure solvent, e is the elementary charge, ε is the relative permittivity of the solvent, and k_B is Boltzmann's constant. Data for the relative permittivity of pure water as a function of temperature were obtained from [49].

Interactions between cations and anions are represented by the functions B_{ij} , B'_{ij} , B_{ij}^ϕ , and C_{ij} :

$$B_{MX} = \beta_{MX}^{(0)} + \beta_{MX}^{(1)} g(\alpha_{MX} \sqrt{I}) + \beta_{MX}^{(2)} g(12\sqrt{I}) \quad (\text{B.3})$$

$$B'_{MX} = \beta_{MX}^{(1)} g'(\alpha_{MX} \sqrt{I})/I + \beta_{MX}^{(2)} g'(12\sqrt{I})/I \quad (\text{B.4})$$

$$B_{MX}^\phi = \beta_{MX}^{(0)} + \beta_{MX}^{(1)} \exp(-\alpha_{MX} \sqrt{I}) + \beta_{MX}^{(2)} \exp(12\sqrt{I}) \quad (\text{B.5})$$

$$C_{MX} = \frac{C_{MX}^\phi}{2|z_M z_X|^{1/2}} \quad (\text{B.6})$$

where $\alpha_{MX} = 2.0$ for j -1 electrolytes and $\alpha_{MX} = 1.4$ for 2-2 and higher electrolytes. The parameters $\beta_{MX}^{(i)}$ are tabulated for a given ion pair, and $\beta_{MX}^{(2)}$ is associated with complex formation and generally only non-zero for 2-2 electrolytes. The functions $g(x)$ and $g'(x)$ are

$$g(x) = 2(1 - (1+x)e^{-x})/x^2 \quad (\text{B.7})$$

$$g'(x) = -\frac{2}{x^2} \left[1 - \left(1 + x + \frac{x^2}{2} \right) e^{-x} \right] \quad (\text{B.8})$$

Interactions between like-charged pairs are represented by Φ_{ij} and Φ'_{ij} :

$$\Phi_{ij} = \theta_{ij} + {}^E\theta_{ij}(I) \quad (\text{B.9})$$

$$\Phi'_{ij} = {}^E\theta'_{ij}(I) \quad (\text{B.10})$$

$$\Phi_{ij}^\phi = \theta_{ij} + {}^E\theta_{ij}(I) + I {}^E\theta'_{ij}(I) \quad (\text{B.11})$$

Here, the only adjustable parameter for a given ion pair is θ_{ij} . The terms ${}^E\theta_{ij}(I)$ and ${}^E\theta'_{ij}(I)$ represent excess free energy arising from electrostatic interactions between asymmetric electrolytes (i.e., ions with charge of like sign and unlike magnitude), and are functions of ionic strength only:

$${}^E\theta_{ij} = \frac{z_i z_j}{4I} \left(J_0(x_{ij}) - \frac{1}{2} J_0(x_{ii}) - \frac{1}{2} J_0(x_{jj}) \right) \quad (\text{B.12})$$

$${}^E\theta'_{ij} = \frac{z_i z_j}{8I^2} \left(J_1(x_{ij}) - \frac{1}{2} J_1(x_{ii}) - \frac{1}{2} J_1(x_{jj}) \right) - \frac{{}^E\theta_{ij}}{I} \quad (\text{B.13})$$

where

$$J_0(x) = \frac{1}{4}x - 1 + \frac{1}{x} \int_0^\infty \left[1 - \exp\left(-\frac{x}{y}e^{-y}\right) \right] y^2 dy \quad (\text{B.14})$$

$$J_1(x) = \frac{1}{4}x - 1 + \frac{1}{x} \int_0^\infty \left[1 - \left(1 + \frac{x}{y}e^{-y} \right) \times \exp\left(-\frac{x}{y}e^{-y}\right) \right] y^2 dy \quad (\text{B.15})$$

and

$$x_{ij} = 6z_i z_j A^\phi \sqrt{I} \quad (\text{B.16})$$

The integrals in Eqs. (B.14) and (B.15) were calculated numerically using MATLAB.

Appendix C. Thermodynamic data

This appendix provides tables of the standard-state Gibbs free energy of formation, the enthalpy of formation, and the molar specific heat capacity for the aqueous and solid compounds considered in the present paper. The standard state is 25 °C and 1 bar. For aqueous species, an additional constraint on the standard state is the usual convention of a hypothetical solution of 1 molal with $\gamma = 1$ (infinitely dilute) or unit activity. The column to the right of each thermodynamic quantity lists the associated reference. The letter ‘C’ in the reference column indicates that the value was estimated according to the procedure outlined in Sec. 3.2.3. Some values of μ° were computed from solubility products or enthalpy and entropy of formation data given in the associated reference.

Table C.3: Standard state thermodynamic data for solid species

Solid Species	μ° , kJ/mol	Ref.	$\Delta_f H^\circ$, kJ/mol	Ref.	C_P° , J/mol-K	Ref.
BaBr ₂	-736.8	[30]	-757.3	[30]		
BaBr ₂ · 2H ₂ O	-1226.0	C	-1361.1	C		
BaCl ₂	-810.9	[50]	-860.1	[50]	75.1	[30]
BaCl ₂ · H ₂ O	-1059.0	[50]	-1164.8	[50]	116.8	C
BaCl ₂ · 2H ₂ O	-1295.8	[50]	-1461.7	[50]	158.5	C
BaCO ₃	-1132.2	[51]	-1210.9	[51]	86.0	[30]
Ba(OH) ₂	-888.3	[50]	-944.7	[30]		
Ba(OH) ₂ · 8H ₂ O	-2792.5	[30]	-3359.9	C		
BaSO ₄	-1362.2	[30]	-1473.2	[30]	101.8	[30]
CaBr ₂	-656.1	[50]	-674.9	[50]		
CaBr ₂ · 6H ₂ O	-2123.7	C	-2486.3	C		
CaCl ₂	-748.1	[51]	-795.8	[51]	72.9	[30]
CaCl ₂ · H ₂ O	-994.1	C	-1109.2	[22]	114.6	C
CaCl ₂ · 2H ₂ O	-1240.1	C	-1402.9	[22]	156.3	C
CaCl ₂ · 4H ₂ O	-1732.0	[20]	-2009.6	[22]	239.8	C
CaCl ₂ · 6H ₂ O	-2215.3	[20]	-2607.9	[22]	323.2	C
CaCO ₃ (Calcite)	-1129.4	[16]	-1207.4	[16]	83.5	[30]
CaCO ₃ (Aragonite)	-1128.3	[16]	-1207.4	[16]	82.3	[52]
Ca(OH) ₂	-897.7	[20]	-986.6	[50]	87.5	[30]
CaSO ₄	-1323.1	[20]	-1423.7	[50]	99.7	[22]
CaSO ₄ · 2H ₂ O	-1798.6	[20]	-2021.1	[50]	186.0	[22]
CoCl ₂	-282.4	[50]	-325.5	[50]	78.5	[22]
CoCl ₂ · H ₂ O	-523.3	C	-615.0	[22]	120.2	C

Table C.3 (cont.): Standard state thermodynamic data for solid species

Solid Species	μ° , kJ/mol	Ref.	$\Delta_f H^\circ$, kJ/mol	Ref.	C_P° , J/mol-K	Ref.
CoCl ₂ · 2H ₂ O	-764.8	[22]	-923.0	[22]	161.9	C
CoCl ₂ · 6H ₂ O	-1725.5	[22]	-2115.4	[22]	328.8	C
CoCO ₃	-639.3	[53]	-713.0	[30]		
Co(OH) ₂	-454.4	[22]	-539.7	[22]		
CoSO ₄	-782.3	[30]	-888.3	[30]		
CoSO ₄ · 7H ₂ O	-2494.5	C	-3001.6	C		
FeBr ₂	-238.1	[30]	-249.8	[30]		
FeCl ₂	-302.2	[51]	-341.7	[51]	76.7	[30]
FeCl ₂ · 2H ₂ O	-791.4	C	-953.1	[22]	160.1	C
FeCl ₂ · 4H ₂ O	-1280.6	C	-1549.3	[22]	243.6	C
FeCO ₃	-666.7	[51]	-737.0	[51]	82.1	[30]
Fe(OH) ₂	-486.5	[54]	-569.0	[54]		
FeSO ₄	-820.9	[55]	-922.6	[50]	100.4	[30]
FeSO ₄ · H ₂ O	-1062.1	C	-1243.7	[22]	142.4	C
FeSO ₄ · 4H ₂ O	-1785.9	C	-2129.2	[22]	268.4	C
FeSO ₄ · 7H ₂ O	-2509.6	[51]	-3014.4	[51]	394.5	[50]
KBr	-380.1	[51]	-393.5	[51]	52.3	[30]
KCl	-408.6	[20]	-436.5	[30]	51.3	[30]
K ₂ CO ₃	-1063.5	[30]	-1151.0	[30]	114.4	[30]
K ₂ CO ₃ · 1.5H ₂ O	-1431.3	[20]	-1603.9	C	177.0	C
KHCO ₃	-867.8	[20]	-963.2	[30]		
KHSO ₄	-1035.1	[20]	-1160.6	[30]		
KOH	-378.9	[51]	-424.7	[51]	68.9	[30]
KOH · 2H ₂ O	-887.4	[22]	-1051.0	[22]	152.3	C
KOH · H ₂ O	-645.2	[22]	-748.9	[22]	110.6	C
K ₂ SO ₄	-1319.8	[20]	-1437.8	[30]	131.5	[30]
LiBr	-342.0	[30]	-351.2	[30]		
LiBr · 2H ₂ O	-840.6	[55]	-962.7	[55]		
LiBr · H ₂ O	-594.3	[55]	-662.6	[55]		
LiCl	-384.4	[30]	-408.6	[30]	48.0	[30]
LiCl · 2H ₂ O	-879.2	C	-1012.5	[55]	131.4	C
LiCl · H ₂ O	-631.8	[50]	-712.6	[50]	89.7	C
Li ₂ CO ₃	-1132.1	[30]	-1215.9	[30]	99.1	[30]

Table C.3 (cont.): Standard state thermodynamic data for solid species

Solid Species	μ° , kJ/mol	Ref.	$\Delta_f H^\circ$, kJ/mol	Ref.	C_P° , J/mol-K	Ref.
LiOH	-438.9	[51]	-484.9	[51]		
LiOH · H ₂ O	-689.5	[50]	-789.8	[50]		
Li ₂ SO ₄	-1321.7	[30]	-1436.5	[30]	117.6	[30]
Li ₂ SO ₄ · H ₂ O	-1566.3	C	-1738.4	C	159.3	C
MgBr ₂	-503.8	[30]	-524.3	[30]		
MgBr ₂ · 6H ₂ O	-2054.3	[50]	-2407.5	[50]		
MgCl ₂	-591.8	[51]	-641.3	[51]	71.4	[30]
MgCl ₂ · H ₂ O	-862.4	[50]	-967.1	[50]	115.3	[22]
MgCl ₂ · 2H ₂ O	-1118.5	[50]	-1280.3	[50]	159.2	[22]
MgCl ₂ · 4H ₂ O	-1633.8	[50]	-1899.5	[50]	241.4	[22]
MgCl ₂ · 6H ₂ O	-2114.8	[20]	-2499.6	[50]	315.1	[22]
MgCO ₃	-1027.4	[20]	-1095.8	[30]	75.5	[30]
MgCO ₃ · 3H ₂ O	-1723.6	[20]	-2001.5	C	200.7	C
MgCO ₃ · 5H ₂ O	-2199.5	[55]	-2605.3	C	284.1	C
Mg(OH) ₂	-831.4	[20]	-924.5	[30]	77.0	
MgSO ₄ · 2H ₂ O	-1672.6	C	-1896.2	[55]	180.4	C
MgSO ₄ · 4H ₂ O	-2174.6	C	-2496.6	[55]	264.2	C
MgSO ₄ · 6H ₂ O	-2631.7	[20]	-3087.0	[55]	348.1	[55]
MgSO ₄ · 7H ₂ O	-2870.2	[20]	-3388.7	[51]	390.0	C
MgSO ₄ · H ₂ O	-1437.3	[20]	-1602.1	[22]	138.4	C
MgSO ₄	-1170.6	[30]	-1284.9	[30]	96.5	[30]
MnCl ₂	-440.5	[30]	-481.3	[30]	72.9	[30]
MnCl ₂ · H ₂ O	-696.2	[22]	-789.9	[22]	114.6	C
MnCl ₂ · 2H ₂ O	-942.2	[22]	-1092.0	[22]	156.3	C
MnCl ₂ · 4H ₂ O	-1423.8	[55]	-1687.4	[55]	239.8	C
MnCO ₃	-816.0	[51]	-889.3	[51]	81.5	[30]
Mn(OH) ₂	-610.4	[50]	-693.7	[50]		
MnSO ₄	-957.3	[51]	-1065.3	[51]	100.4	[55]
MnSO ₄ · 5H ₂ O	-2180.3	C	-2621.7	C	309.0	C
MnSO ₄ · 7H ₂ O	-2669.5	C	-3244.3	C	392.5	C
MnSO ₄ · H ₂ O	-1201.9	C	-1376.5	[55]	142.1	C
NaBr	-349.0	[30]	-361.1	[30]	51.4	[30]
NaBr · 2H ₂ O	-838.2	C	-964.9	C	134.8	C

Table C.3 (cont.): Standard state thermodynamic data for solid species

Solid Species	μ° , kJ/mol	Ref.	$\Delta_f H^\circ$, kJ/mol	Ref.	C_P° , J/mol-K	Ref.
NaCl	-384.2	[20]	-411.0	[50]	50.5	[30]
Na ₂ CO ₃	-1044.4	[30]	-1130.7	[30]	112.3	[30]
Na ₂ CO ₃ · 10H ₂ O	-3427.9	[20]	-4149.7	C	529.5	C
Na ₂ CO ₃ · 7H ₂ O	-2714.3	[20]	-3244.0	C	404.3	C
Na ₂ CO ₃ · H ₂ O	-1286.1	[20]	-1432.6	C	154.0	C
NaHCO ₃	-851.1	[20]	-950.8	[30]	87.6	[30]
NaHSO ₄	-992.8	[30]	-1125.5	[30]		
NaOH	-379.7	[30]	-425.8	[51]	59.5	[30]
NaOH · H ₂ O	-623.4	[50]	-732.9	[50]	90.2	[22]
Na ₂ SO ₄	-1270.1	[20]	-1387.8	[51]	128.2	[22]
Na ₂ SO ₄ · 10H ₂ O	-3646.9	[20]	-4327.3	[51]	545.4	C
SrBr ₂	-695.9	[51]	-717.6	[51]	75.3	[30]
SrBr ₂ · 2H ₂ O	-1185.1	C	-1321.4	C	158.7	C
SrBr ₂ · 6H ₂ O	-2163.5	C	-2529.0	C	325.6	C
SrCl ₂	-781.1	[30]	-828.9	[30]	75.6	[30]
SrCl ₂ · 2H ₂ O	-1282.0	[55]	-1438.0	[50]	159.0	C
SrCl ₂ · 6H ₂ O	-2240.1	[55]	-2623.8	[50]	325.9	C
SrCl ₂ · H ₂ O	-1031.5	C	-1136.8	[50]	117.3	C
SrCO ₃	-1137.6	[51]	-1218.7	[51]	81.4	[30]
Sr(OH) ₂	-893.9	[50]	-959.0	[30]		
SrSO ₄	-1334.3	[50]	-1453.2	[51]		

Table C.4: Standard state thermodynamic data for aqueous species

Aqueous Species	μ° , kJ/mol	Ref.	$\Delta_f H^\circ$, kJ/mol	Ref.	C_P° , J/mol-K	Ref.
Ba ²⁺	-560.8	[30]	-537.6	[30]	-51.5	[56]
BaOH ⁺	-730.5	[30]	-736.0	[57]	-93.7	[57]
Br ⁻	-104.0	[30]	-121.6	[30]	-127.3	[56]
Ca ²⁺	-553.6	[30]	-542.8	[30]	-31.5	[56]
CaCO ₃ ⁰	-1099.8	[58]	-1202.4	[58]	-123.8	[58]
Cl ⁻	-131.2	[30]	-167.2	[30]	-123.2	[56]
Co ²⁺	-54.4	[30]	-58.2	[30]	-32.6	[56]
CoOH ⁺	-234.4	[57]	-286.4	[57]	100.4	[57]
CO ₂ ⁰	-386.0	[59]	-413.8	[59]	243.1	[59]
CO ₃ ²⁻	-527.8	[30]	-677.1	[30]	-290.8	[56]
Fe ²⁺	-78.9	[30]	-89.1	[30]	-33.9	[56]
FeCO ₃ ⁰	-631.7	[51]				
FeHCO ₃ ⁺	-677.1	[51]				
FeOH ⁺	-277.4	[30]	-324.7	[30]	62.8	[57]
H ⁺	0.0	[30]	0.0	[30]	0.0	[56]
H ₂ CO ₃	-607.1	[16]				
HCO ₃ ⁻	-586.8	[30]	-692.0	[30]	-35.4	[56]
HSO ₄ ⁻	-755.9	[30]	-887.3	[30]	22.2	[56]
K ⁺	-283.3	[30]	-252.4	[30]	8.3	[56]
Li ⁺	-293.3	[30]	-278.5	[30]	59.4	[56]
Mg ²⁺	-454.8	[30]	-466.9	[30]	-22.3	[56]
MgCO ₃ ⁰	-999.0	[58]	-1132.1	[58]	-114.6	[58]
MgOH ⁺	-626.7	[30]	-640.0	[57]	128.9	[57]
Mn ²⁺	-228.1	[30]	-220.8	[30]	-17.2	[56]
MnCO ₃ ⁰	-783.9	[51]				
MnHCO ₃ ⁺	-826.0	[51]				
MnOH ⁺	-405.0	[30]	-450.6	[30]	36.4	[57]
Na ⁺	-261.9	[30]	-240.1	[30]	37.9	[56]
OH ⁻	-157.2	[30]	-230.0	[30]	-137.2	[56]
SO ₄ ²⁻	-744.5	[30]	-909.3	[30]	-269.4	[56]
Sr ²⁺	-559.5	[30]	-545.8	[30]	-42.1	[56]
SrCO ₃ ⁰	-1108.2	[58]	-1207.6	[58]	-134.3	[58]